Covariant density functional theory: Reexamining the structure of superheavy nuclei

S. E. Agbemava,[1] A. V. Afanasjev,[1,2] T. Nakatsukasa,[2,3] and P. Ring[4]

[1]*Department of Physics and Astronomy, Mississippi State University, Mississippi 39762, USA*
[2]*Center for Computational Sciences, University of Tsukuba, Tsukuba 305-8577, Japan*
[3]*RIKEN Nishina Center, Wako 351-0198, Japan*
[4]*Fakultät für Physik, Technische Universität München, D-85748 Garching, Germany*

A systematic investigation of even-even superheavy elements in the region of proton numbers $100 \leqslant Z \leqslant 130$ and in the region of neutron numbers from the proton-drip line up to neutron number $N = 196$ is presented. For this study we use the five most up-to-date covariant energy density functionals of different types, with a nonlinear meson coupling, with density-dependent meson couplings, and with density-dependent zero-range interactions. Pairing correlations are treated within relativistic Hartree-Bogoliubov theory based on an effective separable particle-particle interaction of finite range and deformation effects are taken into account. This allows us to assess the spread of theoretical predictions within the present covariant models for the binding energies, deformation parameters, shell structures, and α-decay half-lives. Contrary to the previous studies in covariant density functional theory, it was found that the impact of $N = 172$ spherical shell gap on the structure of superheavy elements is very limited. Similar to nonrelativistic functionals, some covariant functionals predict the important role played by the spherical $N = 184$ gap. For these functionals (NL3*, DD-ME2, and PC-PK1) there is a band of spherical nuclei along and near the $Z = 120$ and $N = 184$ lines. However, for other functionals (DD-PC1 and DD-MEδ) oblate shapes dominate at and in the vicinity of these lines. Available experimental data are, in general, described with comparable accuracy and do not make it possible to discriminate between these predictions.

I. INTRODUCTION

Science is driven by the efforts to understand unknowns. In low-energy nuclear physics many such unknowns are located at the extremes of the nuclear landscape [1–3]. The region of superheavy elements (SHEs), characterized by the extreme values of proton number Z, is one such extreme. Contrary to other regions of the nuclear chart, the SHEs are stabilized only by quantum shell effects. Because of this attractive feature and the desire to extend the nuclear landscape to higher Z values, this region is an arena of active experimental and theoretical studies.

Currently available experimental data reach proton number $Z = 118$ [4,5] and dedicated experimental facilities such as the Dubna Superheavy Element Factory will hopefully make it possible to extend the region of SHEs up to $Z = 120$ and for a wider range on neutron numbers at lower Z values. Unfortunately, even this facility will not be able to reach the predicted centers of the island of stability of SHEs at $(Z = 114, N = 184)$, $(Z = 120, N = 172/184)$ and $(Z = 126, N = 184)$ as given by microscopic + macroscopic (MM) approaches [6–10] or by covariant [11–14] and Skyrme [9,12] density functional theories (DFTs), respectively.

One has to recognize that the majority of systematic DFT studies of the shell structure of SHEs has been performed in the 1990s and at the beginning of the past decade. These studies indicate that the physics of SHEs is much richer in the DFT framework than in MM approaches. This is attributable to self-consistency effects, which are absent in the MM approaches. For example, they manifest themselves by a central depression in the density distribution of spherical SHEs [12,15], which

has not been seen in the MM approaches. Moreover, besides the successful covariant energy density functionals (CEDFs) NL1 [16] and NL3 [17], during the past 10 years a new generation of energy density functionals has been developed both in covariant [18–22] and in nonrelativistic [23,24] frameworks; they are characterized by an improved global performance [3,23,24]. In addition, the experimental data on SHEs became much richer [25,26] in these years.

In such a situation it is necessary to reanalyze the structure of superheavy nuclei using both the full set of available experimental data on SHEs and the new generation of energy density functionals. There are several goals of this study. First, we investigate the accuracy of the description of known SHEs with the new generation of CEDFs and find whether the analysis of existing experimental data makes it possible to distinguish between predictions of different functionals for nuclei beyond the known region of SHEs. Second, the comparative analysis of the results obtained with several state-of-the-art functionals will make it possible to estimate the spreads of theoretical predictions when extending the region of SHEs beyond the presently known, to establish their major sources and to define the physical observables and regions of SHEs which are less affected by these spreads.

This is a very ambitious goal and, as a consequence, several restrictions are imposed. This study is performed only in the framework of covariant density functional theory (CDFT) [27]. We use the CEDFs NL3* [20], DD-ME2 [18], DD-MEδ [22], DD-PC1 [19], and PC-PK1 [21]. They are the state-of-the-art functionals representing the major classes of CEDFs (for

more details see the discussion in Sec. II of Ref. [3]).[1] Moreover, their global performance has recently been analyzed in Refs. [3,28] and they are characterized by an improved description of experimental data as compared with previous generation of CEDFs. Moreover, the study of Refs. [3,29] provides theoretical spreads in the description of known nuclei and their propagation towards the neutron-drip line obtained with four CEDFs (NL3*, DD-ME2, DD-MEδ, and DD-PC1). This is in contrast with earlier studies of SHEs in the CDFT framework based on the functionals whose performance was tested only in very restricted regions of the nuclear chart and for which no analysis of theoretical spreads has been carried out.

Contrary to many earlier CDFT studies of the shell structure in superheavy nuclei restricted to spherical shape, in this investigation the effects of deformation are taken into account. As it will be shown later, neglecting deformation can lead to wrong conclusions because many SHEs are characterized by soft potential energy surfaces with coexisting minima. Considering the numerical complexity of global investigations, we restrict our calculations to axial reflection symmetric shapes. Such calculations are realistic for the absolute majority of the ground states. Octupole deformation does not play a role in the ground states of SHEs [30,31] but it affects the properties of the outer fission barriers [30,32]. In the current paper those are not considered in detail (see the discussion in Sec. IV A). Although triaxiality may play a role in the ground states of some SHEs [33], such cases are rather exceptions than the rule [30,32–34]. Moreover, model predictions for stable triaxial deformation in the ground states vary drastically between the models, even in experimentally known nuclei [35], and are frequently not supported by the analysis of experimental data [36]. In addition, triaxial RHB [37] calculations are at present too time consuming to be undertaken on a global scale. These arguments justify neglecting of triaxiality in the description of the ground states in this investigation.

In addition, we restrict our investigation to even-even nuclei. Unfortunately, no reliable configuration assignments exist for ground states of experimentally known odd-mass SHEs to be confronted with the theory. However, systematic studies of the accuracy of the reproduction of energies of deformed one-quasiparticle states in actinides are available for the CEDF NL3* [38,39].

The paper is organized as follows. Section II describes the details of the calculations. The single-particle structure and shell gaps at spherical shape together with the spreads in their description are discussed in Sec. III. The impact of deformation on the properties of SHEs is considered in Sec. IV. Section V contains the systematics of calculated charge quadrupole deformations. The validity of the δ_{2n} and δ_{2p} quantities as the indicators of shell gaps is discussed in Sec. VI. We report on masses and separation energies in Sec. VII. The α-decay properties are considered in Sec. VIII. Finally, Sec. IX summarizes the results of our work.

II. THE DETAILS OF THE THEORETICAL CALCULATIONS

In the present paper, the RHB framework is used for systematic studies of all $Z = 96$–130 even-even actinides and SHEs from the proton-drip line up to neutron number $N = 196$. The details of this formalism have been discussed in Secs. II–IV of Ref. [3] and Sec. II of Ref. [29]. Thus, we only provide a general outline of the features specific for the current RHB calculations.

We consider only axial and parity-conserving intrinsic states and solve the RHB equations in an axially deformed oscillator basis [40–43]. The truncation of the basis is performed in such a way that all states belonging to the shells up to $N_F = 20$ fermionic shells and $N_B = 20$ bosonic shells are taken into account. As tested in a number of calculations with $N_F = 26$ and $N_B = 26$ for heavy neutron-rich nuclei, this truncation scheme provides sufficient numerical accuracy. For each nucleus the potential energy curve is obtained in a large deformation range from $\beta_2 = -1.0$ up to $\beta_2 = 1.05$ in steps of $\beta_2 = 0.02$ by means of a constraint on the quadrupole moment Q_{20}. Then the correct ground-state configuration and its energy are defined; this procedure is especially important for the cases of shape coexistence.

To avoid the uncertainties connected with the definition of the size of the pairing window, we use the separable form of the finite-range Gogny pairing interaction introduced by Tian *et al.* [44]. Its matrix elements in r space have the form

$$V(\boldsymbol{r}_1,\boldsymbol{r}_2,\boldsymbol{r}_1',\boldsymbol{r}_2') = -G\delta(\boldsymbol{R} - \boldsymbol{R}')P(r)P(r')\frac{1}{2}(1 - P^\sigma), \quad (1)$$

with $\boldsymbol{R} = (\boldsymbol{r}_1 + \boldsymbol{r}_2)/2$ and $\boldsymbol{r} = \boldsymbol{r}_1 - \boldsymbol{r}_2$ being the center of mass and relative coordinates. The form factor $P(r)$ is of Gaussian shape

$$P(r) = \frac{1}{(4\pi a^2)^{3/2}}e^{-r^2/4a^2}. \quad (2)$$

The two parameters $G = 738$ fm^3 and $a = 0.636$ fm of this interaction are the same for protons and neutrons and have been derived in Ref. [44] by a mapping of the ${}^1S_0$ pairing gap of infinite nuclear matter to that of the Gogny force D1S [45].

As follows from the RHB studies with the CEDF NL3* of odd-even mass staggerings, moments of inertia and pairing gaps the Gogny D1S pairing and its separable form [Eq. (1)] work well in actinides (Refs. [3,39,46]). The weak dependence of its pairing strength on the CEDF has been seen in the studies of pairing and rotational properties of actinides in Refs. [13,46], of pairing gaps in spherical nuclei in Ref. [3], and of pairing energies in Ref. [29]. Thus, the same pairing [Eq. (1)] is used also in the calculations with DD-PC1, DD-ME2, DD-MEδ, and PC-PK1. Considering the global character of this study, this is a reasonable choice.

Any extrapolation beyond the known region requires some estimate of theoretical uncertainties. This issue has been

---

[1]Note that the functional PC-PK1 has not been used or discussed in Ref. [3] because global studies with it have been performed by the Peking group in Ref. [28]. It is a state-of-the-art functional for point coupling models with cubic and quartic interactions of zero range [21].

discussed in detail in Refs. [47,48] and in the context of global studies within CDFT in the introduction of Ref. [3]. In the present paper, we concentrate on the uncertainties related to the present choice of energy density functionals which can be relatively easily deduced globally [3]. We therefore define spreads of theoretical predictions for a given physical observable as [3]

$$O(Z,N) = |O_{\max}(Z,N) - O_{\min}(Z,N)|, \qquad (3)$$

where $O_{\max}(Z,N)$ and $O_{\min}(Z,N)$ are the largest and smallest values of the physical observable $O(Z,N)$ obtained with the employed set of CEDFs for the (Z,N) nucleus. Note that these spreads are only a crude approximation to the *systematic* theoretical errors discussed in Ref. [48] because they are due to a very small number of functionals which do not form an independent statistical ensemble. Despite this fact, they provide an understanding of which observables and/or aspects

of many-body physics can be predicted with a higher level of confidence than others for density functionals of the given type. Moreover, it is expected that they will indicate which aspects of many-body problem have to be addressed with more care during the development of next generation of EDFs.

III. SINGLE-PARTICLE STRUCTURES AT SPHERICAL SHAPE

As discussed in the Introduction, superheavy nuclei are stabilized by shell effects, i.e., by a large shell gap or at least a considerably reduced density of the single-particle states. Therefore, for a long time an island of stability has been predicted in the CDFT for very heavy nuclei in the region around the proton number $Z = 120$ [11–14]. Figure 1 shows neutron and proton single-particle spectra of the nuclei $^{292}120$ and $^{304}120$ obtained in spherical relativistic mean-field
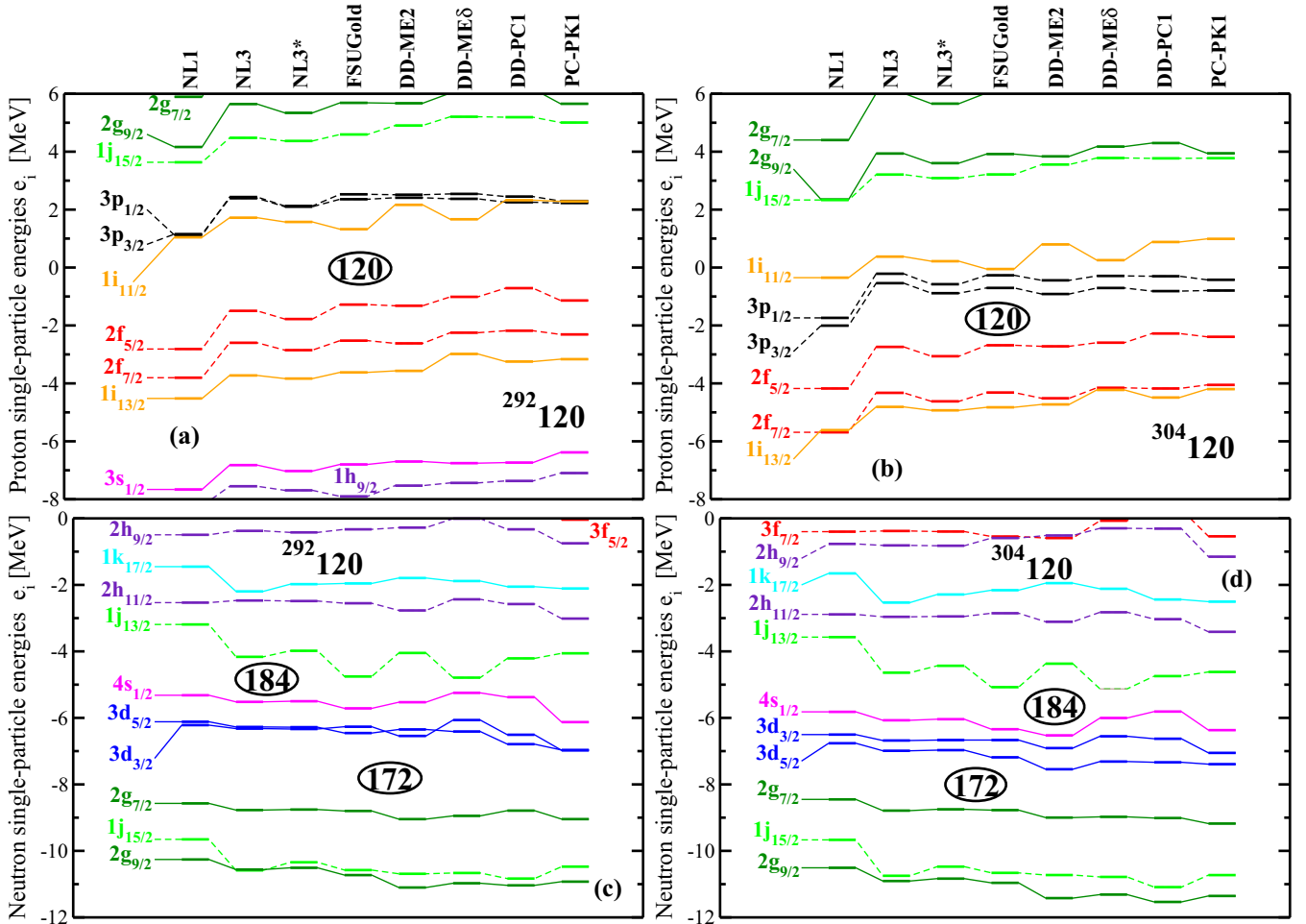

FIG. 1. (Color online) Neutron (bottom panels) and proton (top panels) single-particle states at spherical shape in the SHEs $^{292}120$ and $^{304}120$. They are determined with the indicated CEDFs in RMF calculations without pairing. Solid and dashed connecting lines are used for positive- and negative-parity states. Spherical gaps are indicated. The different CEDFs have been arranged in such a way that we first start from the functionals with a nonlinear σ coupling (NL1 [16], NL3 [17], NL3* [20]), i.e., with a density dependence in the isoscalar channel; then we continue with the functional FSUGold [49], which has, in addition, a nonlinear coupling between ω and ρ mesons and therefore also a density dependence in the isovector channel; then we plot the results for the functionals with explicit density dependent meson-nucleon couplings in all channels (DD-ME2 [18] and DD-MEδ [22]) and finally we end with the point coupling functionals (DD-PC1 [19] and PC-PK1 [21]).

(RMF) calculations. Similar figures have been given for the functionals NL3 and DD-ME2 in Refs. [12,50]. Note that a detailed comparison of several other covariant and nonrelativistic Skyrme functionals is presented in Ref. [12]. In Fig. 1 we show the results for an extended set of eight CEDFs. The global performance of the CEDFs NL3*, DD-ME2, DD-MEδ, and DD-PC1 has been studied in Ref. [3]. The shell gaps at $Z = 120$ and at $N = 172$ are especially pronounced in the nucleus $^{292}120$ (left panels of Fig. 1). This is a consequence of the presence of a central depression in the density distribution generated by a predominant occupation of the high-j orbitals above the occupied single-particle states in ^{208}Pb. Because of their large ℓ values these orbitals produce density at the surface of the nucleus. Filling up the low-j neutron orbitals above the Fermi surface of the $^{292}120$ nucleus on going from $N = 172$ up to $N = 184$ leads to a flatter density distribution in the $N = 184$ system [15]. As a consequence, the $Z = 120$ and $N = 172$ shell gaps are reduced and the $N = 184$ gap is increased (right panels of Fig. 1). As one can see in Fig. 1, these features are rather general and do not depend much on the specific density functional.

Of course, as shown in Fig. 1, there are theoretical uncertainties in the description of the single-particle energies and in their relative positions. The precise size of the large shell gaps depend on the functional. The corresponding spreads are summarized in Fig. 2(a), which shows the average sizes of these shell gaps and the spreads in their predictions. These gaps in the superheavy region are compared with the calculated gaps in lighter doubly magic nuclei, such as ^{56}Ni, ^{100}Sn, ^{132}Sn, and ^{208}Pb.

Because the nuclear radius $R \approx r_0 A^{1/3}$, i.e., the average width of the potential, increases with the mass number A, the shell gaps decrease with $A^{-1/3}$ and by this reason we show in Fig. 2(b) the shell gaps and their spreads scaled with a factor $A^{1/3}$. These scaled shell gaps are considerably more constant with A, but there is still a tendency that even the scaled gaps decrease in general with A. This is probably related to the spin-orbit coupling, which is proportional to the orbital angular momentum ℓ, because it causes an increasing downward shift of the high-j intruder levels. The spreads give some information on the theoretical uncertainties of the sizes of the calculated gaps. Definitely, the impact of these spreads on the model predictions depends on the ratio of their size with respect of the size of calculated shell gaps. The presence of theoretical spreads has less severe consequences on the predictions of spherical nuclei around magic gaps at $Z = 28,50,82$ and $N = 28,50,82,126$ than on similar predictions for SHEs because the former typically have larger shell gaps for comparable theoretical uncertainties. Of course, this is only true in general. The $N = 172$ shell gap in the nucleus $^{292}120$ forms an exception. It is more or less the same for all the CEDFs under consideration and therefore its uncertainty deduced from these spreads is relatively small.

It is evident that the predictive power for new shell gaps in the superheavy region depends on the quality of the description of the single-particle energies of the various CEDFs. Considering Figs. 1 and 2, one can hope that an improvement in the DFT description of the energies of the single-particle
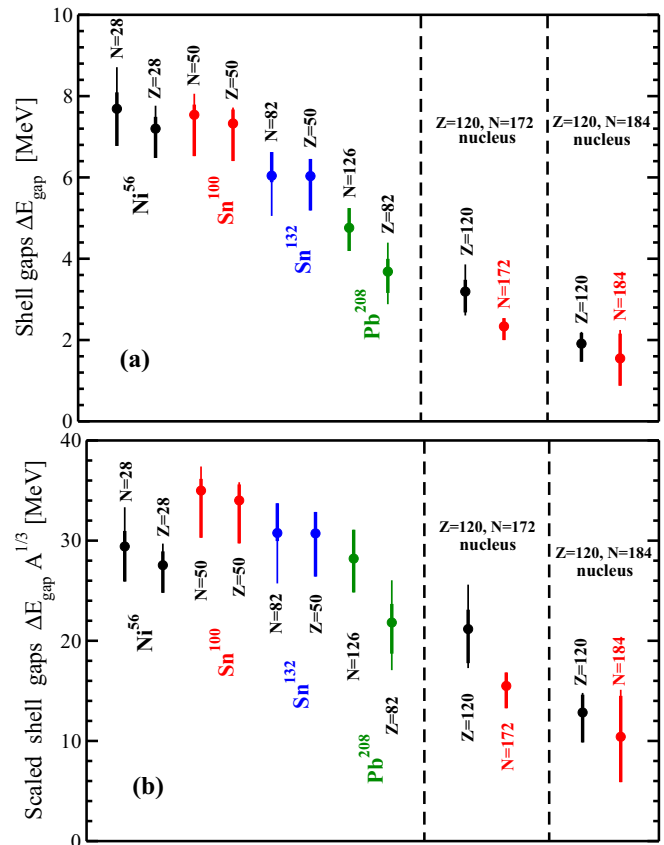

FIG. 2. (Color online) (a) Neutron and proton shell gaps ΔE_{gap} of the indicated nuclei. The average (among ten used CEDFs) size of the shell gap is shown by a solid circle. Thin and thick vertical lines are used to show the spread of the sizes of the calculated shell gaps; the tops and bottoms of these lines correspond to the largest and smallest shell gaps among the considered set of CEDFs. Thin lines show this spread for all employed CEDFs, while thick lines are used for the subset of four CEDFs (NL3*, DD-ME2, DD-MEδ, and DD-PC1). Particle numbers corresponding to the shell gaps are indicated. (b) The same as in panel (a), but with the sizes of the shell gaps and the spreads in their predictions scaled with mass factor $A^{1/3}$.

states in known nuclei will also reduce the uncertainties in the prediction of the shell structure of the SHEs. It is well known that in DFT the single-particle energies are auxiliary quantities and there are problems in their precise description within this framework. It is generally assumed that this has two reasons. First, the coupling of the single-particle motion to low-lying surface vibrations has to be taken into account, and, second, there is not enough known about the influence of additional terms in the Lagrangian, such as tensor forces [51]. Particle-vibrational coupling is particularly large in spherical nuclei. So far, its influence on the accuracy of the description of the single-particle energies and on the sizes of shell gaps has been studied in relativistic particle-vibration [52,53] and quasiparticle-vibration [54] coupling models with the CEDFs NL3 [17] and NL3* [20] only. The experimentally known gaps of ^{56}Ni, ^{132}Sn, and ^{208}Pb are reasonably well described in the relativistic particle-vibration calculations of Ref. [53]. Also, the impact of particle-vibration coupling on spherical
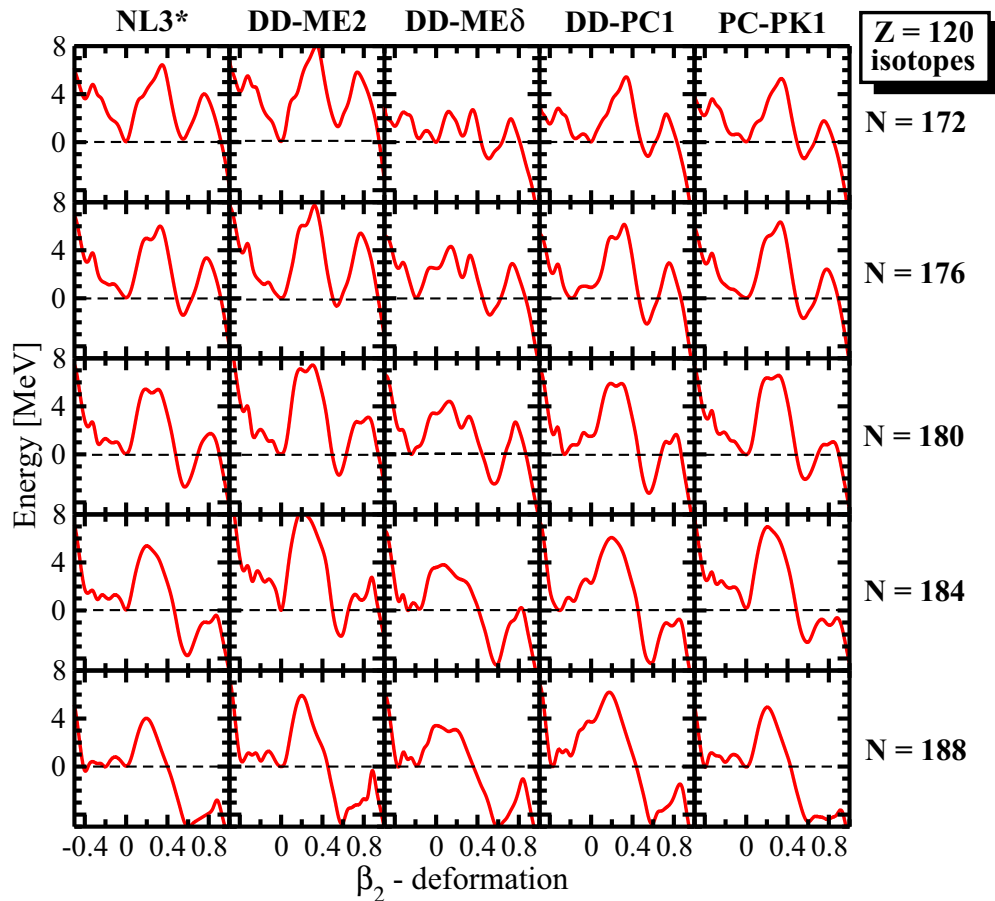
FIG. 3. (Color online) Deformation energy curves for the chain of $Z = 120$ isotopes obtained in axial RHB calculations with the indicated CEDFs. The energy of the spherical or oblate ground states are set to zero.

shell gaps in SHEs has been investigated in Refs. [53,55]. Although this effect, in general, decreases the size of shell gaps, the $Z = 120$ gap still remains reasonably large but there is a competition between the smaller $N = 172$ and $N = 184$ gaps. The accuracy of the description of the energies of one-quasiparticle deformed states in the rare-earth and actinide region has been statistically evaluated in Ref. [38] within the framework of relativistic Hartree-Bogoliubov theory. On the one hand, these studies have proven some success of CDFT: The covariant functionals provide a reasonable description of the single-particle properties despite the fact that such observables were not used in their fit. On the other hand, they illustrate the need for a better description of the single-particle energies.

IV. THE IMPACT OF DEFORMATION ON THE PROPERTIES OF SUPERHEAVY NUCLEI

Although it is commonly accepted that the large spherical shell gaps at $Z = 120$ and $N = 172$ define the center of the island of stability of SHEs for the majority of the covariant functionals [12,13], these conclusions were mostly obtained in investigations restricted to spherical shapes. In addition, some calculations suggest [50,56], or do not exclude [13], the existence of a spherical shell gap at the neutron number

$N = 184$. However, as discussed below, the inclusion of deformation can change the situation drastically for some functionals.

To illustrate this fact, the deformation energy curves of the $Z = 120$ isotopes and the $N = 184$ isotones are presented in Figs. 3 and 4. Here we restrict our considerations to five CEDFs, namely, NL3*, DD-ME2, DD-MEδ, DD-PC1, and PC-PK1, whose global performance is well established [3,28]. In the following discussion we neglect the prolate superdeformed minimum, which is sometimes even lower than the spherical or oblate minimum, because of the reasons discussed in detail in Sec. IV A. In Figs. 3 and 4 the lowest spherical or oblate minimum is considered as the ground state and indicated by a dashed horizontal line. In Fig. 3 we see that the ground states of the $Z = 120$ isotopes with $N = 172$–184 are spherical for NL3*, DD-ME2, and PC-PK1. This is a consequence of the presence of the large $Z = 120$ spherical shell gap (see Fig. 1). For these three functionals, the increase of neutron number N leads to softer potential energy curves for β_2 values between -0.4 and 0.0. As a result, for $N = 188$ an oblate minimum either becomes lowest in energy (for NL3*) or competes in energy with the spherical solution (for DD-ME2 and PC-PK1). This softness of the potential energy curves is even more pronounced for the DD-MEδ and DD-PC1, for which the oblate solution is lower in energy than the
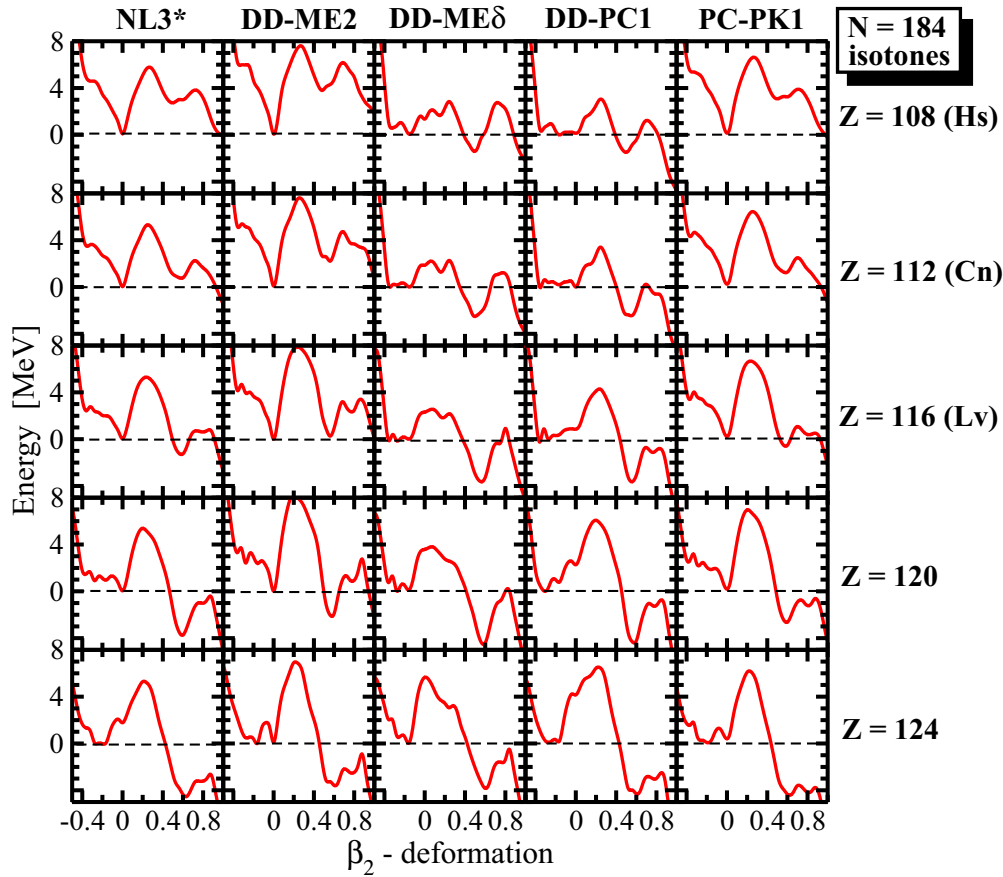
FIG. 4. (Color online) The same as in Fig. 3 but for $N = 184$ isotones.

spherical solution in all displayed nuclei apart from $N = 172$ (Fig. 3).

Although it is tempting to relate this feature to the fact that the size of the $Z = 120$ gap is smallest among the employed functionals for DD-MEδ in the $(Z = 120, N = 172)$ nucleus and for DD-PC1 in the $(Z = 120, N = 184)$ nucleus [see Figs. 1(a) and 1(b)], this explanation is too simplistic. This is because even for the cases when the sizes of the $Z = 120$ gap are very similar (compare, for example, their sizes for DD-ME2 and DD-MEδ in the $(Z = 120, N = 184)$ nucleus [Fig. 1(b)]), the deformations of their minima in the ground state are different. This strongly suggests that the evolution of the single-particle structure with deformation, which leads to negative shell correction energies at oblate shape, is responsible for the observed features. Thus, not only the size of the spherical shell gaps but also the location of the single-particle states below and above these gaps are responsible for the observed features.

This is clearly seen in the Nilsson diagrams presented in Fig. 5 for the nucleus $^{304}120$. Pronounced deformed shell gaps in the proton subsystem are clearly seen for $\beta \sim -0.2$ at $Z = 116, 126$, for $\beta \sim -0.3$ at $Z = 118, 120$, and for $\beta \sim -0.4$ at $Z = 118, 122$. Although, in detail, the size of these deformed gaps, some of which are comparable in magnitude with the $Z = 120$ spherical gap, depends on the functional, they are present both for DD-PC1 and for NL3*.

The most pronounced deformed neutron shell gap is seen at $N = 178$ for $\beta_2 \sim -0.25$; the size of this gap is comparable with the spherical shell gap at $N = 184$. At similar deformations somewhat smaller deformed shell gaps are seen at $N = 184$, 190, and 192.

It is important to recognize that, contrary to the spherical states with a degeneracy of $2j + 1$, deformed states are only twofold degenerate. This will also impact the shell correction energy because it depends on the averaged density of the single-particle states in the vicinity of the Fermi surface [57–59]. As a result, close to the above-discussed deformed shell gaps the negative shell correction energy can be larger in absolute value than the one at spherical shape even for similar sizes of the respective deformed and spherical shell gaps. In the language of the MM approach, this difference can be sufficient to counteract the increase of the energy of the liquid drop with increasing oblate deformation in SHEs [60]. The consequences of this interplay between shell correction and liquid drop energies and the role played by the low-level density of the single-particle states in the vicinity of above-discussed deformed shell gaps are clearly visible in the potential energy curves of the $^{304}120$ nucleus presented in Fig. 3 for DD-PC1 and NL3*. For DD-PC1, the ground state is oblate with deformation $\beta_2 \sim -0.3$. However, two excited minima are also seen at $\beta_2 \sim -0.15$ and $\beta_2 = 0.0$. Although the ground state of the nucleus $^{304}120$ is spherical for NL3*, three minima
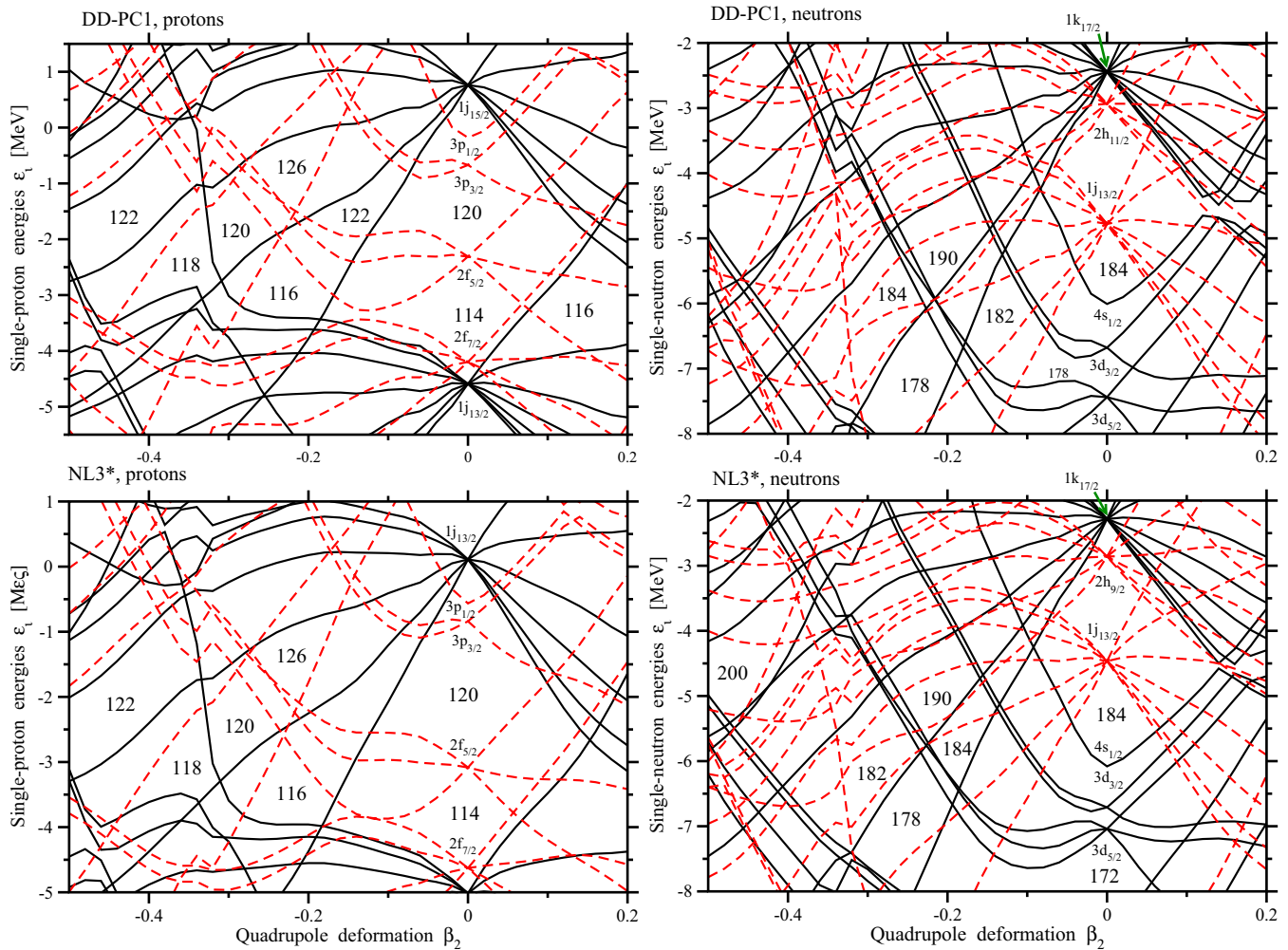
FIG. 5. (Color online) Single-particle energies, i.e., the diagonal elements of the single-particle Hamiltonian h in the canonical basis [61], for the lowest in total energy solution in the nucleus $^{304}120$ calculated as a function of the quadrupole equilibrium deformation β_2 for the two indicated functionals. Solid and dashed lines are used for positive- and negative-parity states, respectively. Relevant spherical and deformed gaps are indicated. Note that the transition from spherical to deformed shapes removes the $2j + 1$ degeneracy of the spherical orbitals. The selected range in deformation is representative for ground-state deformations of the SHEs in the vicinity of the $Z = 120$ and $N = 184$ lines and beyond them.

at $\beta_2 \sim -0.4$, $\beta_2 \sim -0.3$, and $\beta_2 \sim -0.2$ are seen at excitation energies of around 1 MeV. These local minima are the consequence of the fact that the corresponding minima in the proton and neutron shell correction energies correspond to different deformations.

Similar features are also observed for the $N = 184$ isotones in Fig. 4. The nucleus Hs ($Z = 108$) has a well-pronounced spherical minimum for NL3*, DD-ME2, and PC-PK1. For these functionals, the increase of proton number Z leads to an increase of softness in the potential energy surface for $-0.4 \leqslant \beta_2 \leqslant 0$. However, the ground state remains spherical up to $Z = 120$. On the other side, the ground state of the $Z = 124$ nucleus becomes oblate in these three functionals. The situation is completely different for the functionals DD-MEδ and DD-PC1 for which all nuclei shown in Fig. 4 are characterized by soft potential energy curves in the range $-0.4 \leqslant \beta_2 \leqslant 0$ and by oblate ground states.

A. Comment on superdeformed minima and outer fission barriers

The axial RHB calculations restricted to reflection symmetric shapes show that there exists a second [superdeformed (SD)] minimum with deformation of $\beta_2 \sim 0.5$ or higher for all the nuclei under investigation (Figs. 3 and 4). In the nucleus $Z = 120, N = 172$ it is in energy close to the ground state for NL3* and DD-ME2 but lower in energy than the spherical or oblate minimum for DD-MEδ, DD-PC1, and PC-PK1 (see Fig. 3). With the increase of neutron number the SD minimum becomes the lowest in energy in all nuclei (see also Ref. [62]). A similar situation is also observed for the $N = 184$ isotones. In the $Z = 108$ and $Z = 112$ isotopes, the spherical minimum is the lowest in energy for NL3*, DD-ME2, and PC-PK1 (see Fig. 4). With increasing proton number Z, the SD minimum becomes the lowest in energy. The situation is different for DD-MEδ and DD-PC1 because (i) in these functionals the SD

minimum is the lowest in energy in all nuclei shown in Fig. 4 and (ii) the potential energy curves of the $Z = 108, 112,$ and 116 nuclei are much softer (with relatively small inner and outer fission barriers) than in other functionals. It is necessary to conclude that the relative energies of the spherical and/or oblate and SD minima strongly depend on the functional.

Whether these SD states are stable, metastable, or unstable should be defined by the height (with respect of the SD minimum) and the width of the outer fission barrier. The results presented in Figs. 3 and 4 show that while in some nuclei this barrier is appreciable, it is extremely small in others. Moreover, it was demonstrated in systematic RMF + BCS calculations with NL3* for the $Z = 112$–120 nuclei that the inclusion of triaxial or octupole deformation decreases this barrier substantially by 2 to 4 MeV so it is around or less than 2 MeV in the nuclei studied in Ref. [32]. Calculations with DD-PC1 and DD-ME2 for six nuclei centered around $Z = 114, N = 176$ led to similar results [32].

The impact of octupole deformation on the outer fission barriers of SHEs has also been studied in the RMF + BCS calculations with the CEDFs NL3 and NL-Z2 in Ref. [63]. In this work, the SD minima exist in the calculations without octupole deformation (see Fig. 5 in Ref. [63]). Because the heights of outer fission barriers in the axial reflection symmetric calculations are lower in NL-Z2 than in NL3, the inclusion of octupole deformation completely eliminates the outer fission barriers in NL-Z2 but keeps their heights around 2.5 MeV in the NL3 functional. In addition, it was demonstrated in actinides in the RMF + BCS calculations of Ref. [64] that nonaxial octupole deformation can further reduce the height of outer fission barrier by 0.5–1 MeV. A similar effect may be expected also in superheavy nuclei.

Thus, a detailed analysis of the outer fission barriers requires symmetry-unrestricted calculations in the RHB framework which are extremely time consuming. So far no such studies exist. Even the symmetry-unrestricted RMF + BCS calculations (which are at least by one order of magnitude less time consuming than the RHB calculations) have been performed only for actinides [64–66] in which experimental data on outer fission barriers exist. Global symmetry-unrestricted RHB calculations for SHE have to be left for the future. However, from the discussion above it is clear that outer fission barriers are expected to be around 2 MeV or less. The results of Refs. [32,63] do not cover SHE beyond $Z = 120$ and $N = 184$ lines. However, Figs. 3 and 4 show a clear trend for the decrease of the height of outer fission barrier beyond these lines; for these nuclei its height is less than 2 MeV in many functionals even in axially symmetric calculations restricted to reflection symmetric shapes. Thus, it is already clear that the low outer fission barriers with barrier heights around 2 MeV or less existing in the majority of the CDFT calculations discussed above would translate into a high penetration probability for spontaneous fission, such that most likely these SD states (even if they exist) are metastable. Moreover, nonrelativistic calculations usually do not produce a SD minimum and an outer fission barrier in superheavy nuclei [63,67–70].

In addition, existing experimental data on SHE (such as total evaporation-residue cross section or spontaneous fission half-lives) [26] do not show any abrupt deviation from the expected trends which could be interpreted as a transition to a SD ground state.

These are the reasons why we restrict our consideration to the ground states associated with either normal-deformed prolate, oblate, or spherical minima.

V. THE SYSTEMATICS OF THE DEFORMATIONS

The calculated charge quadrupole deformations of the ground states for five CEDFs are plotted in Fig. 6. They are shown for the $Z = 96$–130 nuclei located between the two-proton drip line (see Table IV in Ref. [3]) and $N = 196$. The impact of the large spherical shell gaps discussed in Sec. III on the structure of superheavy nuclei can be accessed via the analysis of the width of the band of spherical nuclei shown by gray color in the (Z, N) chart of Fig. 6. The width of this gray region along a specific particle number corresponding to a shell closure indicates the impact of this shell closure on the structure of neighboring nuclei. For example, for NL3* the width of such a band at $Z \approx 120$ is, on average, three even-even nuclei in the Z direction for $N = 172$–188 and the width of a corresponding band at $N \approx 184$ is, on average, four even-even nuclei in the N direction for $Z = 96$–120. This result is contrary to existing discussions in CDFT, which emphasize the impact of the $N = 172$ shell gap over the $N = 184$ gap. Our results clearly show that the effect of the $N = 184$ spherical shell gap on the equilibrium deformation is more pronounced as compared with the $N = 172$ gap. A similar situation exists in the calculations with PC-PK1 [see Fig. 6(e)]. However, the impact of the $Z = 120$ and the $N = 184$ spherical shell gaps becomes less pronounced for DD-ME2 [see Fig. 6(b)].

The impact of the $Z = 120$ spherical shell gap is significantly reduced for DD-MEδ and DD-PC1; only the $N = 172$ nuclei with $Z = 118$ and 120 are spherical for those two functionals. The impact of the $N = 184$ shell gap is also considerably decreased; the ground states of the $N = 184$ nuclei are spherical only for $Z \leqslant 102$ in DD-MEδ and for $Z \leqslant 112$ in DD-PC1 [see Figs. 6(c) and 6(d)]. Note also that the band of spherical nuclei around $N = 184$ is narrow for DD-PC1. These results are in contradiction to the expectation that the large size of the spherical $Z = 120$ gap in Fig. 1 forces the isotopes with $Z = 120$ to be spherical for a large range of neutron numbers. Note that proton and neutron shell gaps act simultaneously in the vicinity of a nucleus with proton and neutron numbers corresponding to those gaps. Thus, the effect of a single gap is more quantifiable away from this nucleus.

It is interesting to compare these results with the ones obtained for $Z \leqslant 104$ nuclei in Fig. 17 of Ref. [3] with NL3*, DD-ME2, DD-MEδ, and DD-PC1. In these nuclei the neutron $N = 82, 126,$ and 184 shell gaps have a more pronounced effect on the nuclear deformations as compared with the proton shell gaps at $Z = 50$ and $Z = 82$. This feature was common to all the CEDFs used in Ref. [3]. However, the width of the band of spherical and near-spherical nuclei along these neutron numbers was broader in NL3* as compared with other functionals under consideration. We see the same feature also in superheavy nuclei along the $N = 184$ shell closure (see Fig. 6); note that PC-PK1 was not used in Ref. [3].
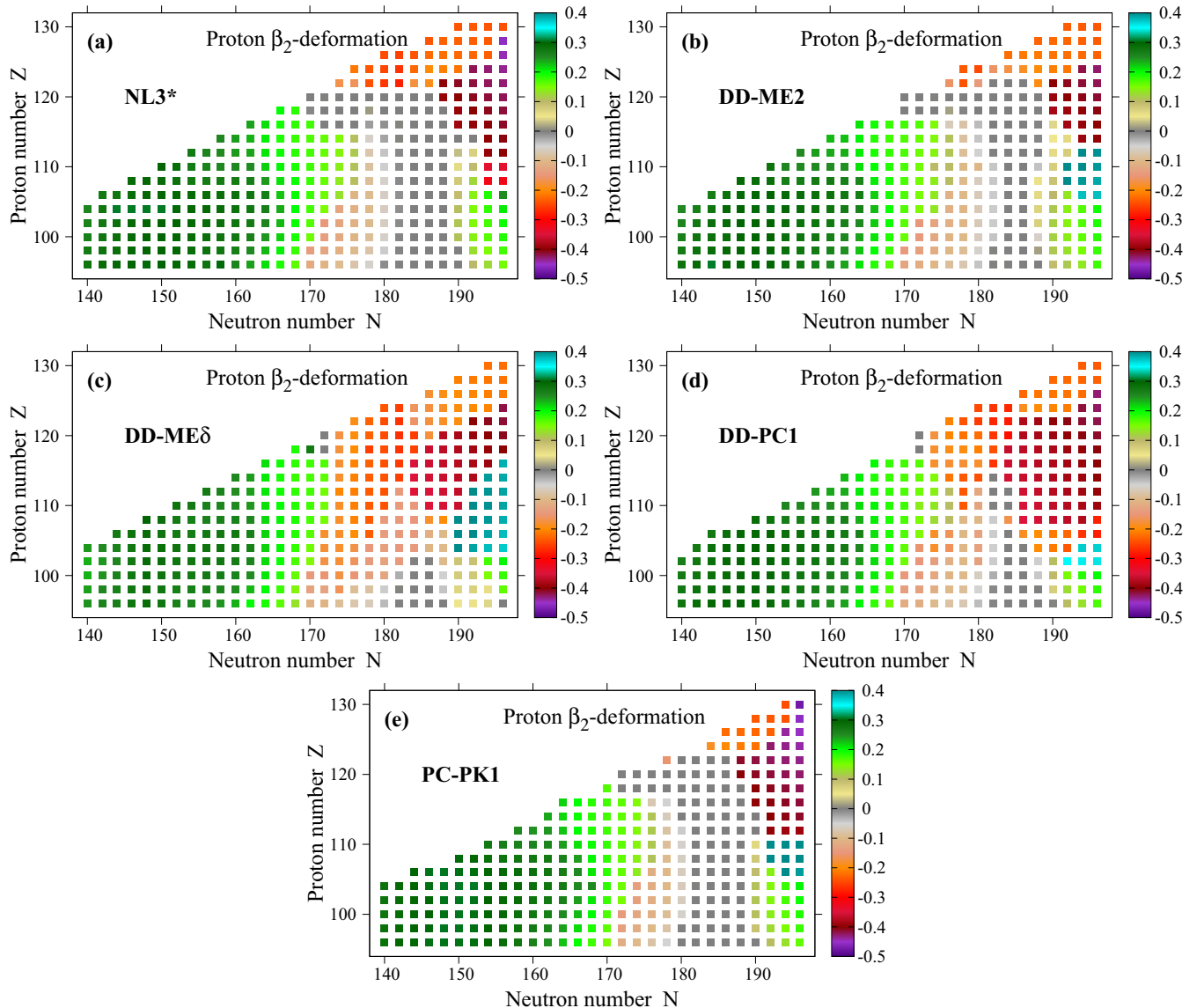
FIG. 6. (Color online) Charge quadrupole deformations β_2 obtained in the RHB calculations with the indicated CEDFs. Note that ground-state equilibrium deformations of the $N = 182$ nuclei with $Z = 106$ and 116 and of the $N = 184$ nuclei with $Z = 108$, 114, 116, and 118 obtained with DD-PC1 [Fig. 6(d)] differ from the ones shown in the bottom panel of Fig. 4 in Ref. [72]. This is a consequence of the use of a smaller deformation range ($-0.4 \leqslant \beta_2 \leqslant 1.0$) and a larger step in deformation ($\Delta\beta_2 = 0.05$) in the RHB calculations of Ref. [72] as compared with the present paper.

The RHB results for superheavy nuclei show the unusual feature that the ground states of the nuclei outside the band of spherical or near-spherical shapes (shown by gray color in Fig. 6) have oblate shapes for NL3*, DD-ME2, and PC-PK1. This is contrary to the usual situation observed in the lighter nuclei (see, for example, Fig. 17 in Ref. [3]), where, between shell closures, the nuclei change their shape with increasing particle numbers from spherical to prolate, then to oblate, and finally back to spherical. It is interesting to see that the systematic MM calculations of Ref. [71] based on the Woods-Saxon potential also show a similar preponderance of oblate shapes in the ground states of superheavy nuclei. These MM results were also confirmed by the calculations for a few nuclei performed within Skyrme DFT with the functional

SLy6 [71]. The situation is even more drastic for the CEDFs DD-MEδ (DD-PC1) in which no (or very limited) indications of spherical shapes are seen on passing through the nuclei with $Z = 120$ or $N = 184$. When comparing our results with other calculations, one has to keep in mind that not all published results extend to a sufficiently large deformation for oblate shapes (see, for example, Ref. [70]).

Figure 7 shows the map of calculated charge quadrupole deformations with experimentally known nuclei indicated by open circles. One can see that, apart from the $Z = 116, 118$ nuclei, the predictions of these two functionals (PC-PK1 and DD-PC1) for the equilibrium deformations of experimentally known even-even nuclei are very similar. For these nuclei, PC-PK1 predicts the gradual transition from prolate to spherical
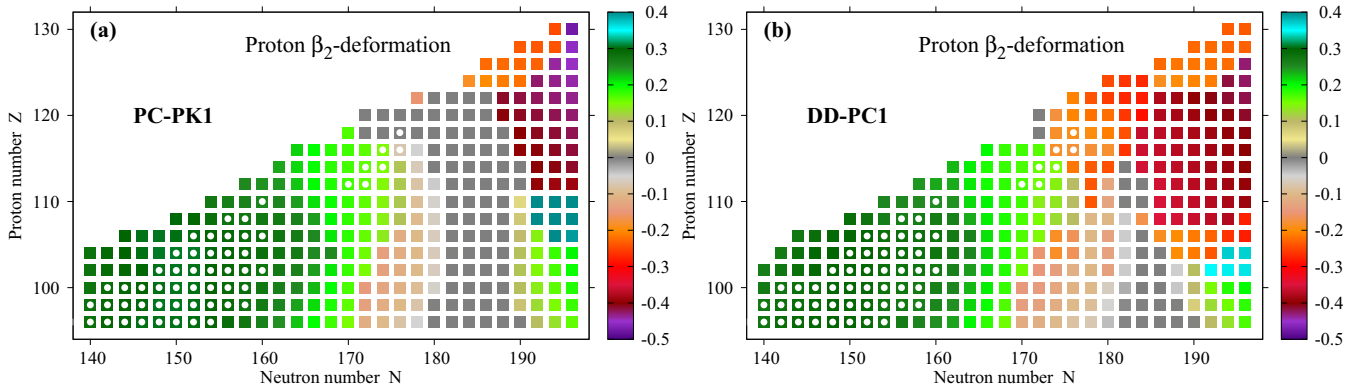
FIG. 7. (Color online) The same as Fig. 6 but with experimentally known nuclei shown by open circles. Only the results with PC-PK1 and DD-PC1 are shown. The information on experimentally known nuclei is taken from Refs. [26,73]. Note that the region of experimentally known superheavy nuclei is broader at high Z when odd and odd-odd mass nuclei are included (see Fig. 2 in Ref. [26]).

shape on going from $Z = 114$ to $Z = 118$. The same happens also for NL3* and DD-ME2 [Figs. 6(a) and 6(b)]. On the contrary, for DD-PC1 the transition from the prolate to the oblate minimum is predicted for experimentally known nuclei on going from $Z = 114$ to $Z = 116$ and all experimentally known $Z \geqslant 116$ nuclei are expected to be oblate. The same happens also for DD-MEδ. However, because of the limited scope of experimental data these differences in the description of experimentally known $Z = 116$ and 118 nuclei between DD-PC1/DD-MEδ and PC-PK1/NL3*/DD-ME2 cannot be discriminated.

Spreads in the theoretical predictions of the charge quadrupole deformations are shown in the left panel of Fig. 8. They are very small in the region of known nuclei and for $N < 170$. Only very few experimentally known nuclei with $Z = 114$, 116, and 118 are located in the region where substantial theoretical spreads exist (compare Fig. 8 with Fig. 7). However, as discussed above, available experimental data on these nuclei do not make it possible to discriminate between different predictions. Quite large spreads exist in the region near the $Z = 120$ and $N = 184$ lines. This is because spherical ground states are predicted in this region by NL3*, DD-ME2, and PC-PK1, while DD-MEδ and DD-PC1 favor oblate shapes in these nuclei. Very large spreads exist in the $Z \sim 110, N \geqslant 190$ region; this is a region where a transition from prolate to oblate shape is seen in the calculations and it takes place at different positions in the (Z, N) chart for the different functionals (see Fig. 6). The theoretical spreads become small again in the upper right corner of the chart; here they are substantial only in several nuclei (shown by green color), which form a "line" parallel to the two-proton drip line. This line is a consequence of the fact that the transition from ground-state deformations $\beta_2 \sim -0.2$ to $\beta_2 \sim -0.4$ takes place for different functionals at different positions in the (N, Z) chart (see Fig. 6).

The right panel of Fig. 8 shows theoretical spreads for the case when the functional DD-MEδ is excluded from consideration. This functional provides unrealistically low heights of inner fission barriers in SHEs [74] and thus it is very unlikely that this functional is appropriate for the region of SHEs. However, its exclusion from consideration reduces only slightly the theoretical spreads.

It is interesting to compare the results of the present analysis of theoretical spreads in the description of ground-state deformations with the global analysis presented in Ref. [3] for $Z \leqslant 104$ nuclei. It is clear that the region of SHEs in the vicinity of the $Z = 120$ and $N = 184$ lines bears the mark
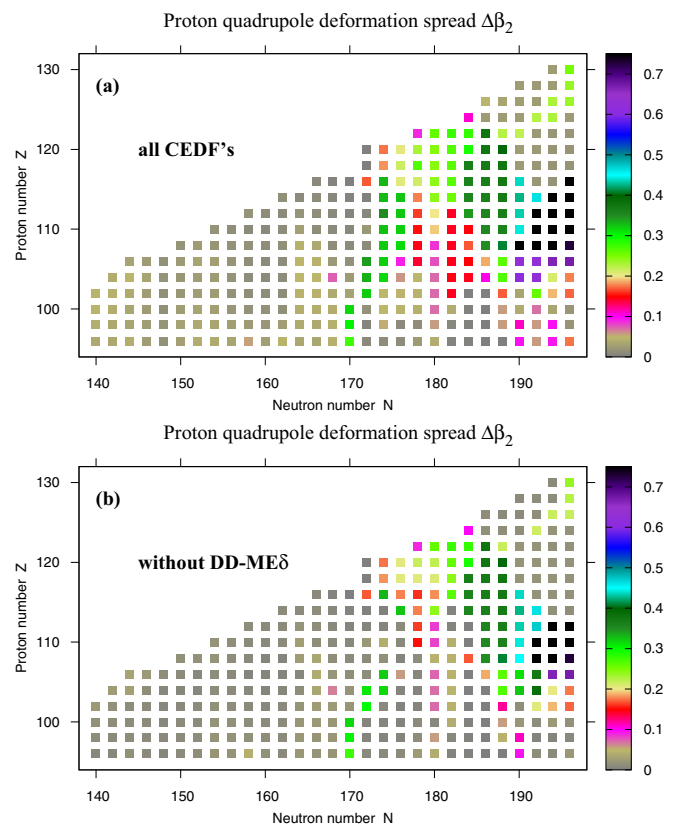

FIG. 8. (Color online) Proton quadrupole deformation spreads $\Delta\beta_2$ as a function of proton and neutron number. $\Delta\beta_2(Z, N) = |\beta_2^{\max}(Z, N) - \beta_2^{\min}(Z, N)|$, where $\beta_2^{\max}(Z, N)$ and $\beta_2^{\min}(Z, N)$ are the largest and smallest proton quadrupole deformations obtained with the set of CEDFs used for the nucleus (Z, N). Panel (a) shows the results for all functionals, while DD-MEδ is excluded in the results shown on panel (b).

of a transitional region characterized either by soft potential energy surfaces or by shape coexistence. This is the source of large theoretical spreads in the prediction of ground-state deformations which exist not only in the region of SHEs but also globally (see Ref. [3]). Both in SHEs and globally these uncertainties are attributable to the deficiencies of the current generation of functionals with respect to the description of single-particle energies.

VI. THE QUANTITIES $\delta_{2n}(Z,N)$ AND $\delta_{2p}(Z,N)$ AS INDICATORS OF SHELL GAPS

The analysis of the shell structure (and shell gaps) of superheavy nuclei is most frequently based on the quantity $\delta_{2n}(Z,N)$ defined as (Ref. [12,13])

$$\delta_{2n}(Z,N) = S_{2n}(Z,N) - S_{2n}(Z,N+2)$$
$$= -B(Z,N-2) + 2B(Z,N) - B(Z,N+2). \quad (4)$$

Here $B(Z,N)$ is the binding energy and $S_{2n}(Z,N)$ is the two-neutron separation energy. The quantity $\delta_{2n}(Z,N)$, being related to the second derivative of the binding energy as a function of the neutron number, is a more sensitive indicator of the local decrease in the single-particle density associated with a shell gap than the two-neutron separation energy $S_{2n}(Z,N)$. This quantity is frequently called as *two-neutron shell gap*. In a similar way, for protons, $\delta_{2p}(Z,N)$ is defined as

$$\delta_{2p}(Z,N) = S_{2p}(Z,N) - S_{2p}(Z+2,N)$$
$$= -B(Z-2,N) + 2B(Z,N) - B(Z+2,N). \quad (5)$$

However, as discussed in detail in Ref. [13], many factors beyond the size of the single-particle shell gap contribute to $\delta_{2n}(Z,N)$ and $\delta_{2p}(Z,N)$, as for instance deformation and pairing changes. For example, the global analysis of these quantities in Ref. [29] shows that for some (Z,N) values $\delta_{2n}(Z,N)$ becomes negative because of deformation changes. Because by definition the shell gap has to be positive, it is clear that the quantities $\delta_{2n,2p}(Z,N)$ cannot serve as explicit measures of the size of the shell gaps.

Unfortunately, in the majority of cases the analysis of these quantities in superheavy nuclei (and thus the conclusions about the underlying shell structure and the gaps) is based on the results of spherical calculations (see, for example, Refs. [12,14,50]). Thus, the possibility of a considerable softness of the potential energy surface leading to a deformed minimum is ignored from the beginning. An alternative way to analyze the shell structure is via the microscopic shell correction energy (see, for example, Ref. [56]). However, such an analysis is also frequently limited to spherical shapes (Ref. [56]) and, in addition, the comparison with experiment is less straightforward.

The danger of a misinterpretation of the structure of superheavy nuclei based on the analysis of the quantities $\delta_{2n}(Z,N)$ and $\delta_{2p}(Z,N)$ obtained in spherical calculations is illustrated in Fig. 9 on the example of DD-PC1. In spherical calculations, the quantity $\delta_{2n}(Z,N)$ has pronounced maxima at $N=184$ for $Z=96$–110 and less pronounced maxima at $N=172$ for $Z=112$–120. Note that in this functional the nucleus ($Z=120, N=172$) is located beyond the two-proton

drip line. However, it is clear that the impact of the $N=172$ shell gap does not propagate far away from $Z=120$. The quantity $\delta_{2p}(Z,N)$ is enhanced in a broad region around $Z=116$–120 and has a maximum for $Z=120$ which becomes especially pronounced approaching $N=172$.

However, in deformed RHB calculations, the quantities $\delta_{2n}(Z,N)$ and $\delta_{2p}(Z,N)$ show a picture in many respects quite different from the one obtained in spherical calculations. In addition to the maxima in the quantity $\delta_{2n}(Z,N)$ at $N=184$ for $Z=96$–108, which are already seen in spherical calculations, deformed RHB calculations show maxima at $N=162$ (for $Z=96$–112) and at $N=148$ (for $Z=98$–102). The latter gap appears for a number of covariant functionals instead of the experimentally observed $N=152$ gap (see Refs. [39] for details). Note that the maxima in $\delta_{2n}(Z,N)$ seen at $N=172$ in spherical calculations disappear in deformed RHB calculations. In addition, some isolated peaks in the quantity $\delta_{2n}(Z,N)$ appear across the nuclear chart of Fig. 9(d) at specific values of Z and N. In many cases, they originate from rapid deformation changes in going from one nucleus to another.

Even more drastic differences are seen when comparing the quantities $\delta_{2p}(Z,N)$ obtained in spherical and in deformed RHB calculations. Any indication of the $Z=120$ spherical shell gap clearly visible in the spherical case [Fig. 9(c)], disappear in deformed calculations [Fig. 9(d)]. This is a consequence of the fact that apart from the $Z=118,120$ nuclei with $N=172$, which are spherical in the ground state, all other nuclei in the vicinity of the $Z=120$ line are oblate in the ground state [see Fig. 6(d)]. The maxima in the quantity $\delta_{2n}(Z,N)$ obtained in deformed RHB calculations are located at completely different Z values as compared with spherical calculations, indicating a possible lowering of the single-particle level density at these values. For example, the high values of the quantity $\delta_{2p}(Z,N)$ seen at $Z=104$ around $N=150$ are attributable to deformed the $Z=104$ shell gap which exists for a number of CEDFs [13,39].

These results clearly illustrate the danger of misinterpretation of the structure of superheavy nuclei when using results of spherical calculations. The presence of large spherical shell gaps will definitely manifest itself in the increase of the relevant $\delta_{2n}(Z,N)$ or $\delta_{2n}(Z,N)$ quantities. However, the restriction to spherical shapes does not make it possible to access the softness of the potential energy surfaces and the presence of large shell gaps at deformation.

VII. MASSES AND SEPARATION ENERGIES

In Table I we list the rms deviations $\Delta E_{\rm rms}$ between theoretical and experimental binding energies for the nuclei with $Z \geqslant 96$; experimental masses from the AME2012 mass evaluation [75] are used here. The masses given in the AME2012 mass evaluation [75] can be separated into two groups. One represents nuclei with masses defined only from experimental data; the other contains nuclei with masses depending in addition on either interpolation or short extrapolation procedures. These procedures involve some degree of subjectivity but has proven to provide a quite accurate estimate in absolute majority of the cases as seen from the comparison
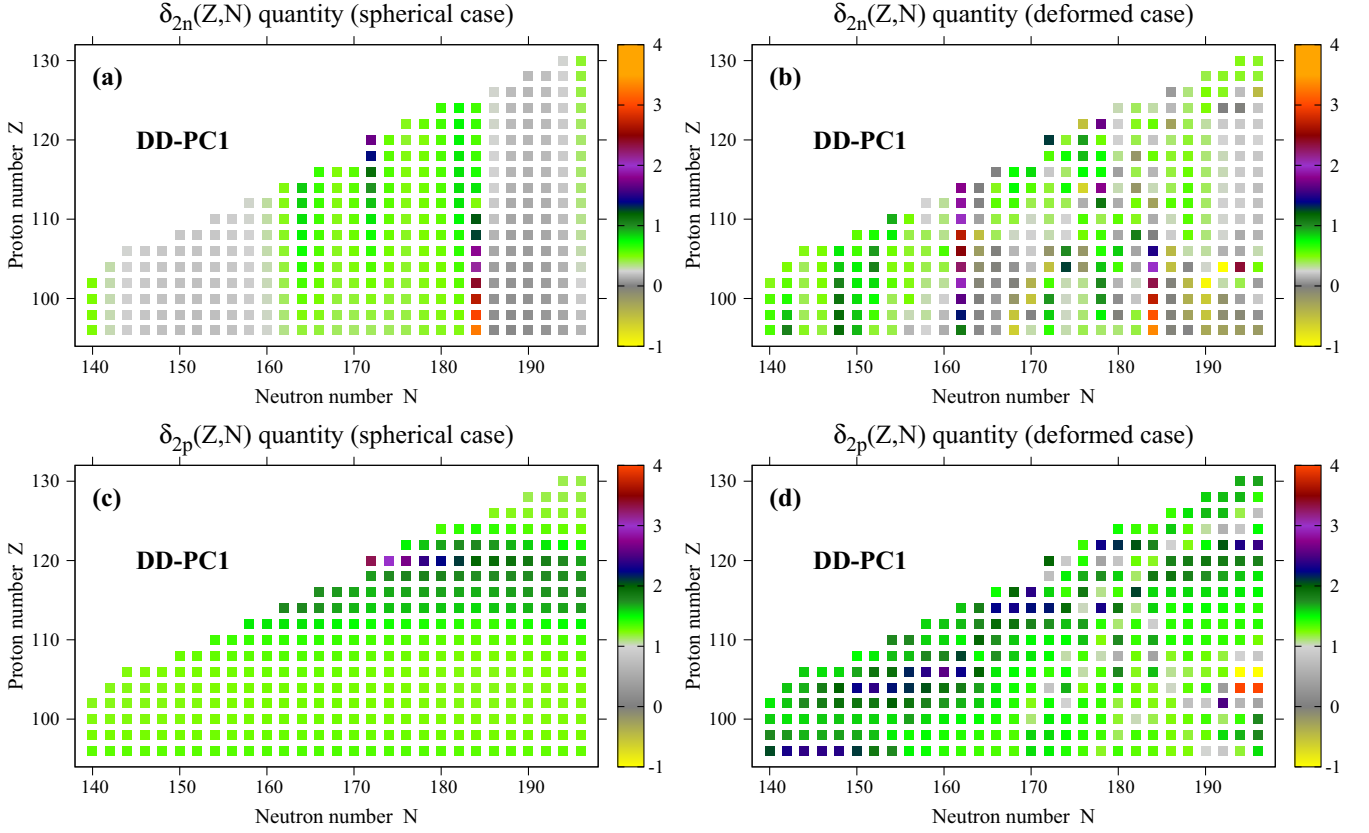
FIG. 9. (Color online) The comparison of the quantities $\delta_{2n}(Z,N)$ (top panels) and $\delta_{2p}(Z,N)$ (bottom panels) obtained in spherical (left panels) and deformed (right panels) RHB calculations with DD-PC1. Note that for clarity of the presentation, the color maps for the quantities $\delta_{2p}(Z,N)$ for protons and $\delta_{2n}(Z,N)$ for neutrons are different.

of these estimates with newly measured masses [76]. For simplicity, we refer to the masses of the nuclei in the first and second groups as measured and estimated. Estimated masses frequently involve the ones for unknown nuclei and they are estimated from the trends in mass surfaces [76]. Note that these mass surfaces also incorporate the information on odd and odd-mass SHEs which are more abundant than their even-even counterparts [26]. Experimental physical observables which depend only on measured masses are shown later by solid symbols in the figures, while the ones which involve at least one estimated mass by open symbols.

For each employed functional the accuracy of the description of the sets of measured and measured + estimated masses is comparable and does not change substantially when the estimated masses are added to the measured ones (see Table I). The same is true for the quantities that depend on the mass differences such as the two-neutron (two-proton) separation energies and the Q_α values. This fact is important because the measured masses represent only 41% in the set of measured + estimated masses used here. It adds additional support to the estimation procedures used in Refs. [76] because global studies of Ref. [3] indicate that CDFT has a good

TABLE I. Root-mean-square deviations $\Delta E_{\rm rms}$, $\Delta(S_{2n})_{\rm rms}[\Delta(S_{2p})_{\rm rms}]$, $\Delta(Q_\alpha)_{\rm rms}$, and $\Delta(\tau_\alpha)_{\rm rms}$ between calculated and experimental binding energies E, two-neutron(-proton) separation energies S_{2n} (S_{2p}), Q_α values, and α-decay half-lives τ_α. The values of physical observables in columns 2–5 are presented in the format "A/B", where A are the values obtained from only measured masses and B are those obtained from measured + estimated masses. Note that only experimental data on even-even nuclei with $Z \geqslant 96$ are used here. In the last column, the deviations are given in terms of orders of magnitude. In each column, boldface is used to indicate the functional with the best rms deviation.

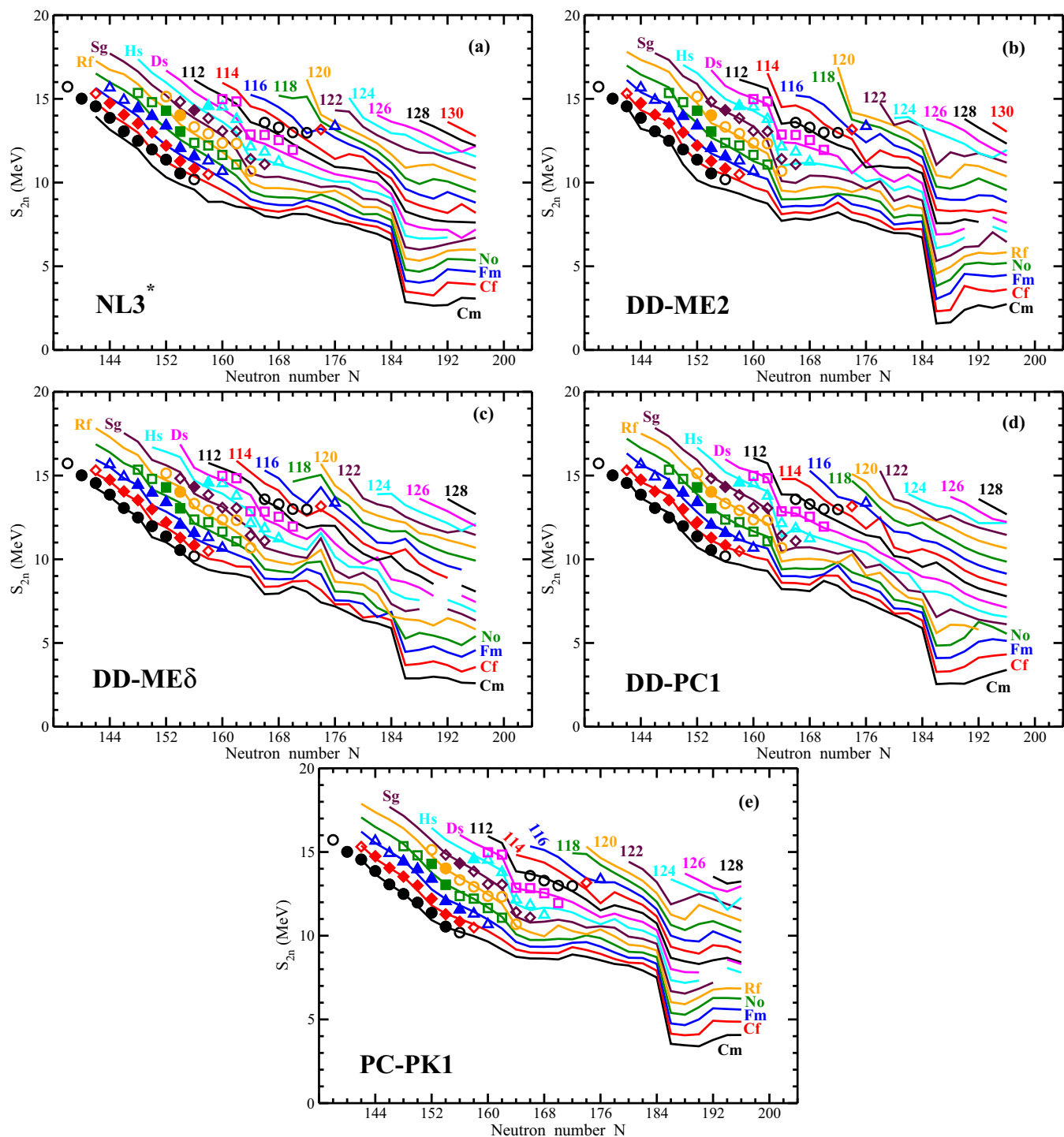| CEDF	$\Delta E_{\rm rms}$ (MeV)	$\Delta(S_{2n})_{\rm rms}$ (MeV)	$\Delta(S_{2p})_{\rm rms}$ (MeV)	$\Delta(Q_\alpha)_{\rm rms}$ (MeV)	$\Delta(\tau_\alpha)_{\rm rms}$ (order)
1	2	3	4	5	6
NL3*	3.02/3.39	0.71/0.68	1.33/1.34	0.68/0.75	2.44
DD-ME2	1.39/1.40	0.45/0.54	0.85/0.90	0.51/0.65	1.95
DD-MEδ	2.52/2.45	0.60/0.51	0.45/0.48	0.39/0.51	1.39
DD-PC1	**0.59/0.74**	0.30/0.32	0.41/0.42	0.36/0.47	1.40
PC-PK1	2.82/2.63	**0.25/0.23**	**0.36/0.33**	**0.32/0.38**	**1.26**

FIG. 10. (Color online) Two-neutron separation energies $S_{2n}(Z,N)$ given for different isotopic chains as a function of neutron number. The experimental data are shown by the symbols and the calculated results by the lines; the same color is used for both quantities belonging to the same isotopic chain. Solid symbols are used for the $S_{2n}(Z,N)$ values determined from measured masses, and open symbols for those including at least one estimated mass. The measured and estimated masses are from Ref. [75]. The transition to a prolate minimum with $\beta_2 \sim 0.35$ in nuclei with $N \sim 192$ (see Fig. 6) creates the jumps in $S_{2n}(Z,N)$; these jumps are not shown and are detectable in the graphs by the breakage of the line.

predictive power in the regions of deformed nuclei with no shape coexistence and the absolute majority of the superheavy nuclei for which measured and estimated masses are provided in Ref. [75] belong to this type of region.

As compared with the global analysis of Refs. [3,28], the accuracy of the description of masses is better for DD-PC1 and DD-ME2, comparable for DD-MEδ and PC-PK1, and worse for NL3*. The best accuracy is achieved for DD-PC1.
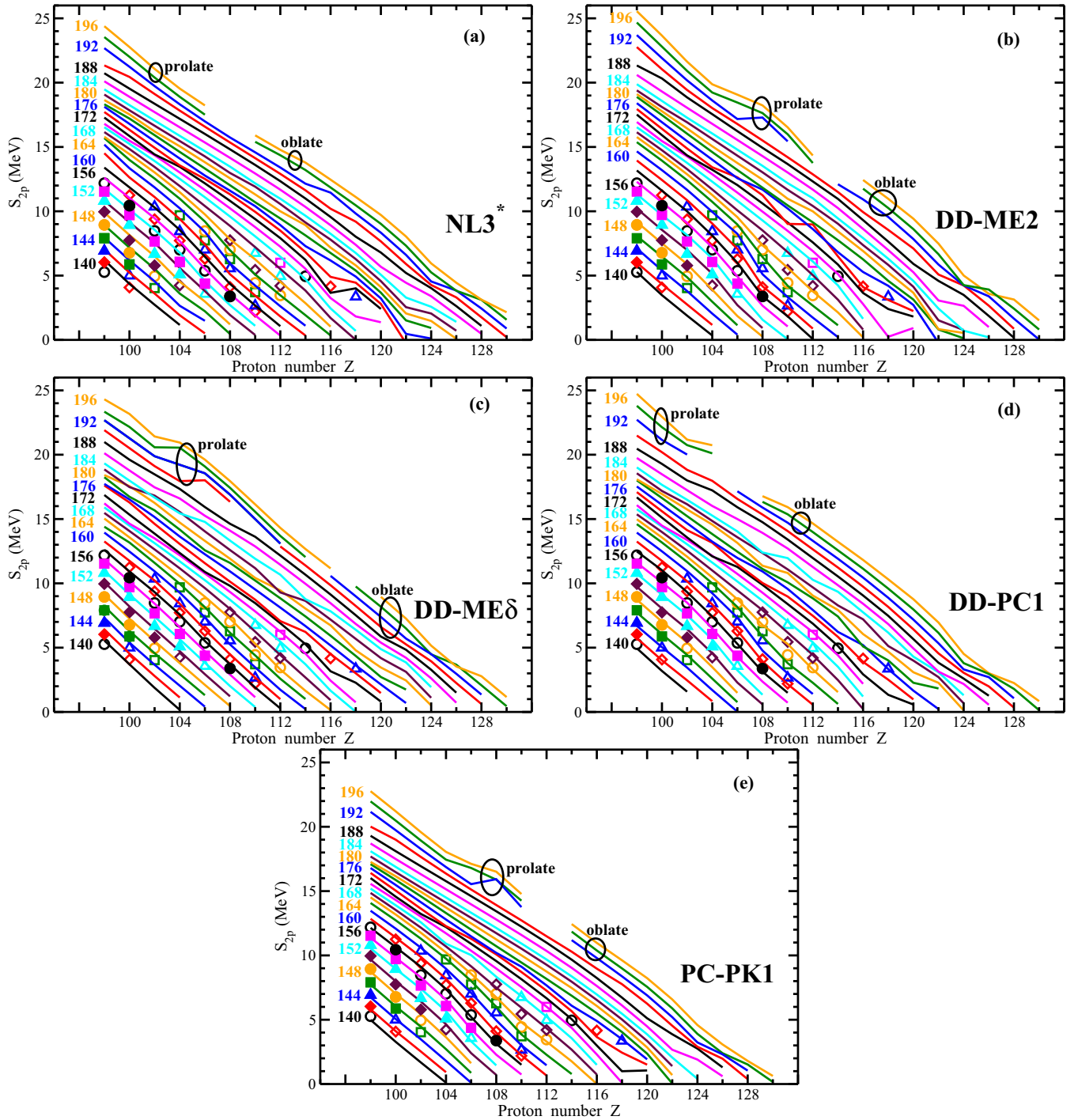
FIG. 11. (Color online) The same as Fig. 10 but for two-proton separation energies $S_{2p}(Z,N)$ given for different isotonic chains as a function of the proton number. The shapes of the nuclei on the different sides of the $N = 188$–196 chains (see Fig. 6) are indicated; the circles envelop the isotone chains which are affected by sharp prolate-oblate transitions. This transition creates the jumps in $S_{2p}(Z,N)$; these jumps are not shown and are detectable in the graphs by the breakage of the line.

This is not surprising considering that this functional has been carefully fitted to the binding energies of deformed rare-earth nuclei and actinides in Ref. [19]. With respect to masses it outperforms other functionals in these regions (see Figs. 6 and 7 in Ref. [3]).

Because our investigation is restricted to even-even nuclei, we consider two-neutron $S_{2n} = B(Z,N-2) - B(Z,N)$ and

two-proton $S_{2p} = B(Z-2,N) - B(Z,N)$ separation energies. Here $B(Z,N)$ stands for the binding energy of a nucleus with Z protons and N neutrons. Apart of the proton subsystem in NL3* and DD-ME2 and the neutron subsystem in NL3*, the two-neutron S_{2n} and the two-proton S_{2p} separation energies are described with a typical accuracy of 0.5 MeV (Table I). This is better by a factor of two than the global accuracy of

around 1 MeV obtained for these functionals in Ref. [3]. The accuracy of the description of separation energies depends on the accuracy of the description of mass differences. As a result, the functional that provides the best description of masses does not always give the best description of two-particle separation energies.

Figures 10 and 11 present a detailed comparison of calculated and experimental two-neutron and two-proton separation energies. While providing, in general, comparable descriptions of experimental data, the calculated results differ in details. The experimental data for the Rf, Sg, Hs, and Ds isotopes clearly show a sharp decrease of the two-neutron separation energies at $N = 162$, which is due to the deformed shell gap at this particle number. This decrease is best described by PC-PK1 [Fig. 10(e)]. DD-ME2 and DD-PC1 overestimate this decrease somewhat [Figs. 10(b) and 10(d)] and NL3* underestimates its size. In contradiction to experiment, DD-MEδ does not show the presence of a gap at $N = 162$ but gives a small deformed shell gap at $N = 164$ [Fig. 10(c)].

It is important to recognize that the conclusions about the deformed $N = 162$ shell gap are based on the comparison with two-neutron separation energies extracted from estimated masses. However, this gap is present both in the macroscopic + microscopic calculations of Refs. [8,77,78] and the DFT calculations based on the Gogny D1S force of Ref. [70]. In addition, from the analysis of experimental data, there are indications about the presence of this gap that suggest that the deformed $N = 162$ shell gap is much larger than the $N = 152$ gap discussed below [76].

For higher N values there are indications of the presence of the $N = 184$ spherical shell gap. However, there is a substantial difference between the functionals on how far this gap propagates into the region of superheavy nuclei. For example, PC-PK1 and DD-ME2 show the propagation of this gap up to $Z \approx 120$ [Figs. 10(b) and 10(e)]. However, this gap is visible only up to the Rf/No region for DD-MEδ and DD-PC1 [Figs. 10(b) and 10(e)]. The results for NL3* are between of these two extremes [Figs. 10(a)].

Contrary to the neutron subsystem, experimental two-proton separation energies are smoother as a function of proton number without clear indications of pronounced shell gaps (Fig. 11). One should note that there exist small deformed shell gaps at $Z = 100$ and $N = 152$ in heavy actinides and/or light superheavy nuclei [13]. They are barely visible in the two-particle separation energies (see Figs. 10 and 11 and Ref. [13]) and are usually seen in the quantities $\delta_{2n}(Z,N)$ and $\delta_{2p}(Z,N)$ (see Sec. VI).

Figures 12 and 13 show that these deformed gaps at $Z = 100$ and $N = 152$ are not reproduced in the CEDFs under consideration. Indeed, the calculations with NL3*, DD-ME2, DD-MEδ, and DD-PC1 place them at $N = 148$ and $Z = 104$. These gaps are clearly seen in the nobelium region in the Nilsson diagrams for NL3* (see Fig. 3 in Ref. [39]). On the contrary, a neutron gap is seen at $N = 154$ and no proton gap exists in the calculations with DD-MEδ. These problems exist also in the description of experimental deformed gaps with the older generation of the CEDFs used in Ref. [13]. They place a neutron gap either at $N = 148$ (NL3, NLRA1, and NL-Z) or at
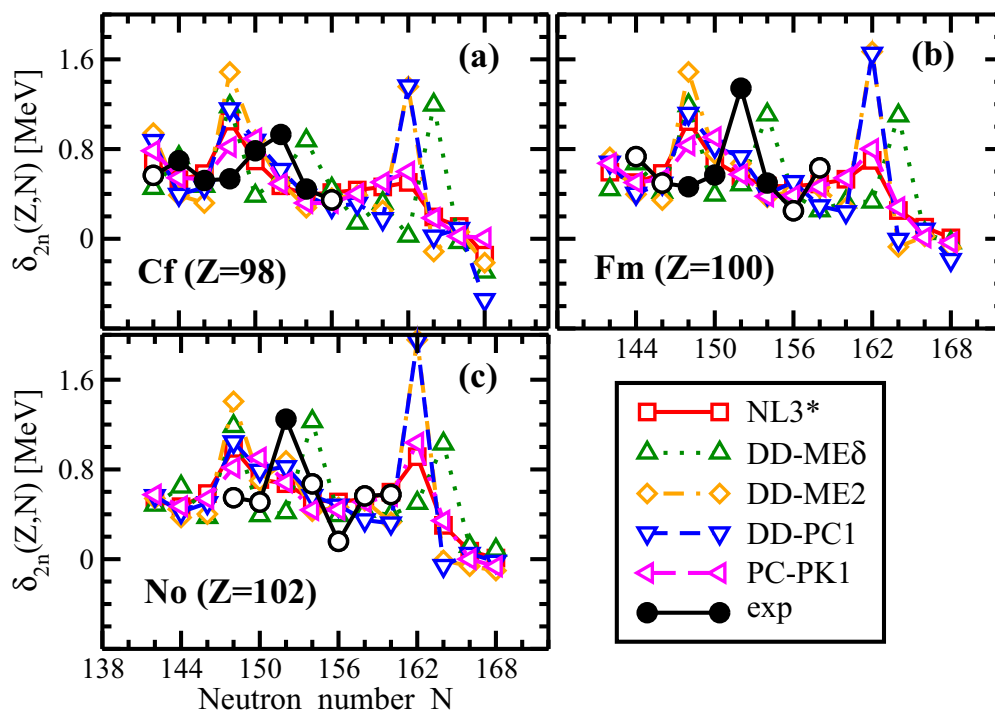

FIG. 12. (Color online) The quantity $\delta_{2n}(Z,N)$ for the Cf, Fm, and No isotope chains. The experimental data (circles) are compared with the results (open symbols) obtained in deformed RHB calculations with the indicated CEDFs. Solid circles are used for the $\delta_{2n}(Z,N)$ values which are determined from measured masses and open circles for those the definition of which involves at least one estimated mass. The measured and estimated masses are from Ref. [75].
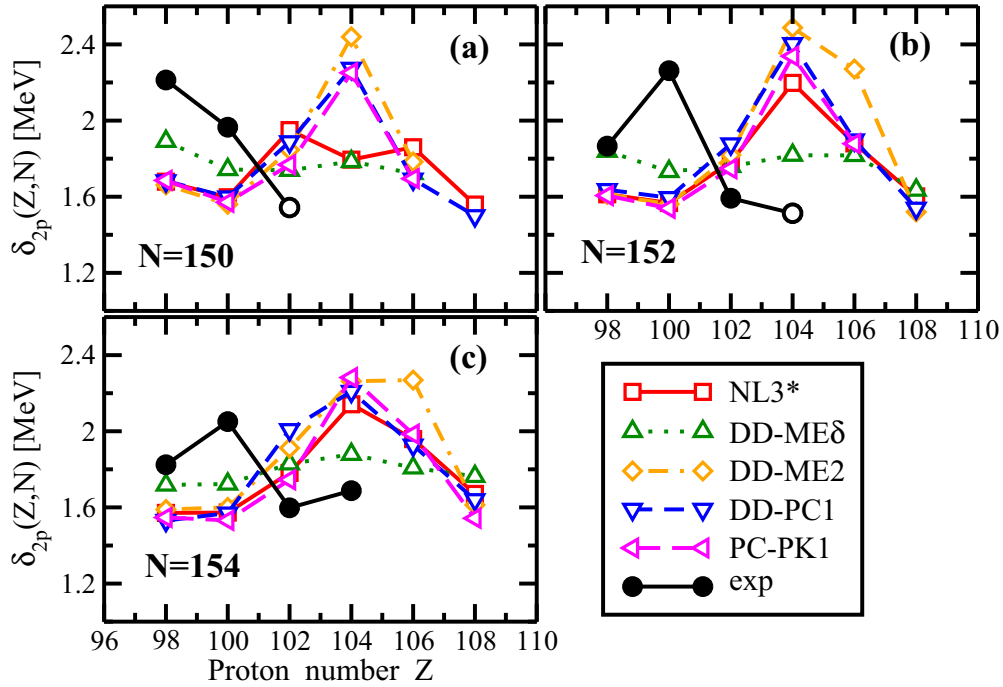
FIG. 13. (Color online) The same as Fig. 12 but for the quantity $\delta_{2p}(Z,N)$ in the $N = 150$, 152, and 154 isotone chains.

$N = 150$ (NL1 and NL-Z) or do not show a gap at all (NLSH). In the same way, a proton gap is placed at $Z = 104$ (NL3, NL1, and NL-Z) or does not exist in NLRA1. Only NLSH predicts a proton gap at the right Z value but it is placed between wrong states [13]. Note that this problem is not specific only for covariant functionals; most of the Skyrme functionals also fail to reproduce these gaps (Refs. [79,80]).

VIII. α-DECAY PROPERTIES

In superheavy nuclei spontaneous fission and α emission compete and the shortest half-life determines the dominant decay channel and the total half-life. Only in cases where the spontaneous fission half-life is longer than the half-life of α emission can superheavy nuclei be observed in experiment. In addition, only nuclei with half-lives longer than $\tau = 10 \ \mu$s are observed in experiments.

The α-decay half-live depends on the Q_α values which are calculated according to

$$Q_\alpha = E(Z,N) - E(Z-2,N-2) - E(2,2), \quad (6)$$

with $E(2,2) = -28.295\,674$ MeV [75] and Z and N representing the parent nucleus.

The RHB results for the Q_α values are compared with experiment in Fig. 14 and the corresponding rms deviations are listed in Table I. Based on the results presented in this table, the best agreement is obtained for PC-PK1 closely followed by DD-PC1 and DD-MEδ and then by DD-ME2 and NL3*. However, a detailed analysis of these results presented in Fig. 14 clearly indicates that DD-MEδ completely misses both the position in neutron number and the magnitude of the peak at $N = 164$ seen in the experimental data for the Rf, Sg, Hs, and Ds isotope chains. Note, however, that the

magnitude of the peak in the experimental data is based on the estimated masses. This peak is a consequence of the deformed $N = 162$ shell gap which is not reproduced in this functional (see Sec. VII). The other functionals correctly place this peak at $N = 164$. The best reproduction of the magnitude of this peak is obtained for PC-PK1. The CEDFs DD-PC1 and DD-ME2 (NL3*) somewhat overestimate (underestimate) its magnitude, reflecting the accuracy of the reproduction of the size of the $N = 162$ shell gap in these CEDFs (see Sec. VII).

The comparison of experimental data with theoretical Q_α values obtained with the covariant functionals (Fig. 14 of the present manuscript and Fig. 18 of Ref. [82]) and with those obtained by nonrelativistic models (see, for example, Fig. 18 in Ref. [82] and Figs. 44 and 45 of Ref. [78]) clearly indicates that the available experimental data do not make it possible to distinguish between the predictions of different models with respect to the position of the center of the island of stability.

The α-decay half-lives were computed using the phenomenological Viola-Seaborg formula [83]

$$\log_{10}\tau_\alpha = \frac{aZ + b}{\sqrt{Q_\alpha}} + cZ + d \quad (7)$$

with the parameters $a = 1.640\,62$, $b = -8.543\,99$, $c = -0.194\,30$, and $d = -33.9054$ of Ref. [84].

The comparison of calculated and experimental half-lives for the α decays is presented in Fig. 15. One can see that reasonable agreement is obtained for all functionals especially for the case of PC-PK1. However, the local increase above the general trend of the experimental half-lives near $N = 152$ visible in the Cf, Fm, and No isotope chains, which is due to the deformed $N = 152$ shell gap, is not reproduced. Neither of the functionals reproduce the position of this gap (see Sec. VII). For higher neutron numbers all functionals predict an increase
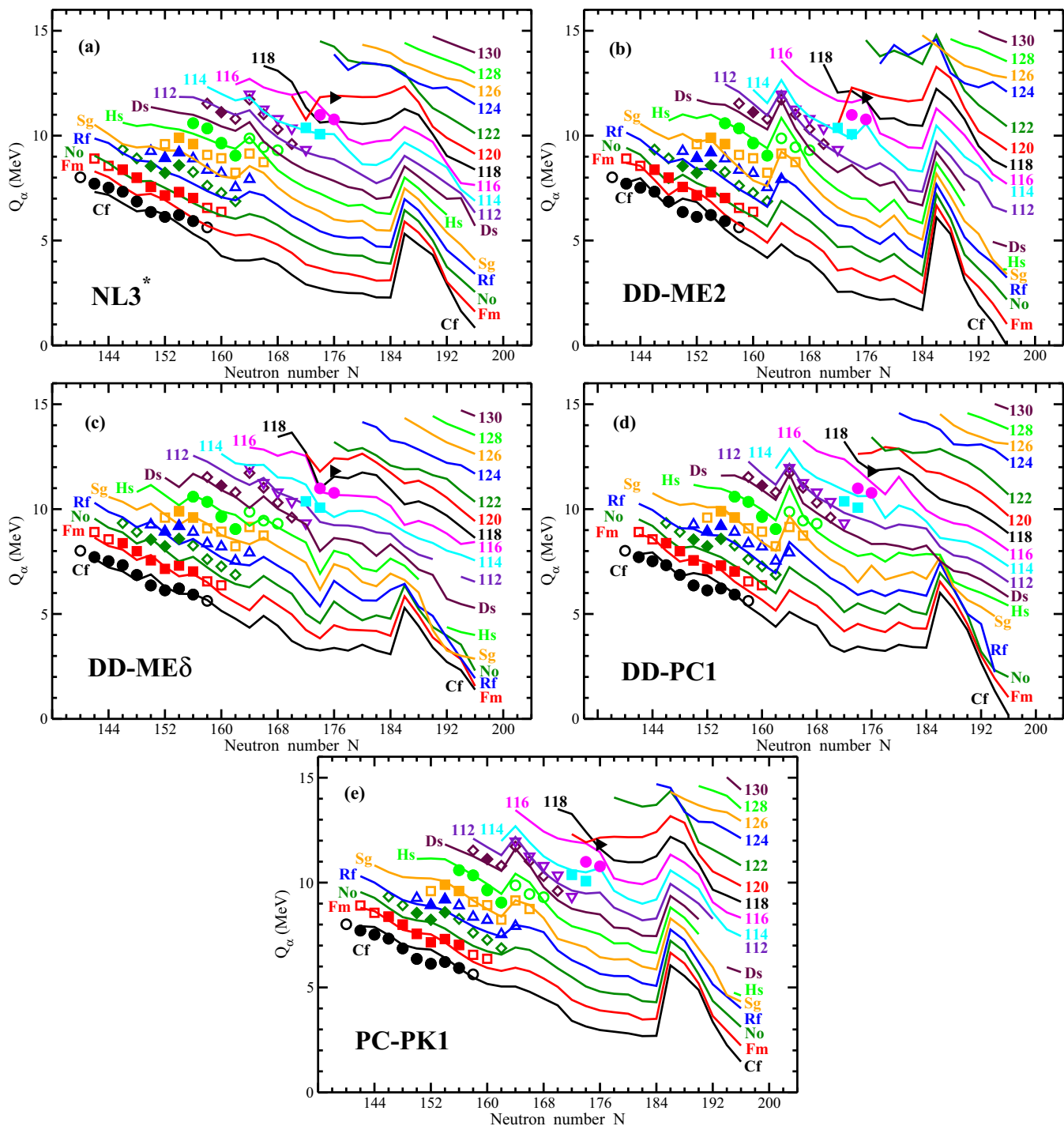
FIG. 14. (Color online) The comparison of experimental and calculated Q_α values for even-even superheavy nuclei. The experimental and calculated values are shown by symbols and lines, respectively. For a given isotope chain, the same color is used for both types of values. Experimental Q_α values are from Ref. [75]. Solid symbols are used for experimentally measured Q_α values [75], which are determined either from measured masses (for low-Z values) or from α-decays (for high-Z values). Open symbols are used for the Q_α values, the determination of which involves at least one estimated mass.

of the half-lives as a function of neutron number N. This trend, however, is interrupted in the vicinity of the spherical shell gap with $N = 184$. For some isotope chains a drastic decrease of the half-lives is observed. It is a consequence of the well-known fact that for nuclei with two neutrons outside a closed shell α-particle emission is easier than for the other nuclei in the same isotopic chain [85]. However, above $N = 184$ the trend of increasing half-lives with the increase of neutron number is restored. The impact of the $N = 184$ shell gap on the α-decay half-lives clearly correlates with the impact of this gap of the deformations of the ground states (Sec. V). In SHEs with high Z values its impact on the α-
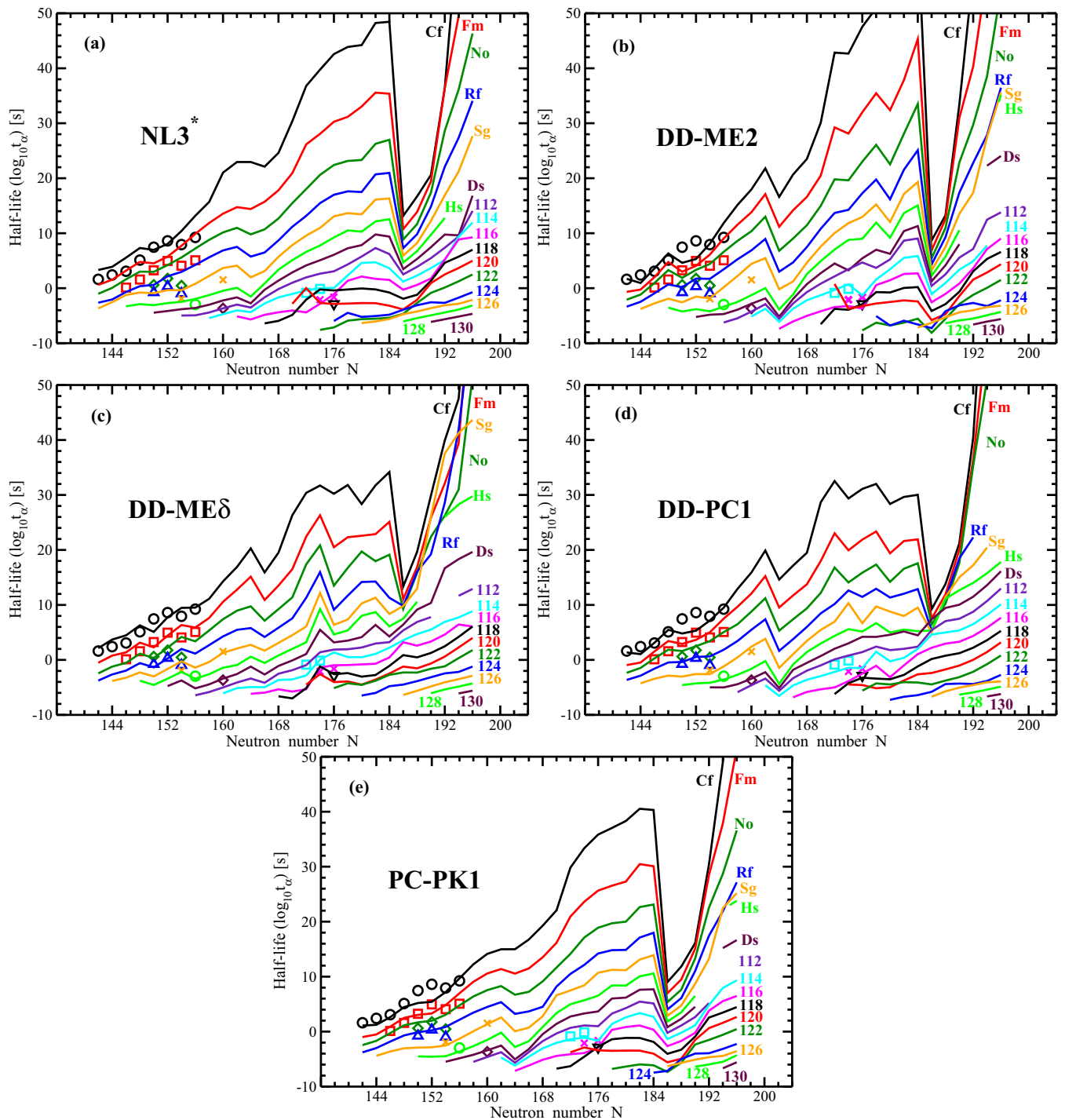
FIG. 15. (Color online) Experimental and calculated half-lives for α decays of even-even superheavy nuclei. The experimental and calculated values are shown by symbols and lines, respectively. For a given isotope chain, the same color is used for both types of values. The experimental data are from Ref. [81].

decay half-lives is either substantially decreased or completely vanishes.

In the region under investigation the magnitude of the α decay half-lives varies in a very wide range from 10^{-8} up to 10^{50} s (or even higher for the Cf, Fm, and No nuclei with $N \sim 190$). For some SHEs with high Z values the calculated half-lives fell below the experimental observation limit of 10^{-5} s.

Despite the fact that the existing experimental data on the α-decay half-lives is described with comparable accuracy by the different functionals, for unknown regions of the nuclear chart there are some cases of substantial difference in their predictions. The most extreme difference is seen in the Cf isotopes, where NL3* and DD-ME2 differ from DD-MEδ and DD-PC1 by approximately 20 orders of magnitude at neutron number

$N = 184$ and slightly below it. However, apart from the $N = 184$ region, the differences in the predictions of different functionals is smaller for SHEs with $Z \sim 114$, where it reaches only few orders of magnitude (Fig. 15). In the $N = 184$ region of these nuclei the differences between predictions of different functionals increase by additional few orders of magnitude. However, above $Z = 120$ these differences decrease with increasing proton number because of the diminishing role of the $N = 184$ spherical shell gap. For example, the differences in the predicted α-decay half-lives do not exceed two orders of magnitude for the $Z = 128$ and 130 nuclei.

IX. CONCLUSIONS

The performance of CEDFs in the region of superheavy nuclei has been assessed using the state-of-the-art functionals NL3*, DD-ME2, DD-MEδ, DD-PC1, and PC-PK1. They represent major classes of covariant functionals with different basic model assumptions and fitting protocols. The available experimental data on ground-state properties of even-even nuclei have been confronted with the results of the calculations. For the first time, theoretical spreads in the prediction of physical observables have been investigated in a systematic way in this region of the nuclear chart for covariant density functionals. Special attention has been paid to the propagation of these spreads towards unknown regions of higher Z values and of more neutron-rich nuclei.

The main results of this work can be summarized as follows.

(i) So far, the absolute majority of investigations of the shell structure of SHEs has been performed in spherical calculations. In the framework of CDFT, these calculations always indicate a large proton shell gap at $Z = 120$, a smaller neutron shell gap at $N = 172$, and, for some functionals, a neutron shell gap at $N = 184$. However, the restriction to spherical shapes does not make it possible to access the softness of the potential energy surfaces and the presence of competing large shell gaps at deformation. As illustrated in the present paper, this restriction has led to a misinterpretation of the shell structure of SHEs. The detailed analysis, with deformation included, shows that the impact of the $N = 172$ shell gap is very limited in the (Z, N) space for all functionals under investigation. The impact of the $Z = 120$ and $N = 184$ spherical shell gaps depend drastically on the functional. It is most pronounced for NL3* and PC-PK1 and is (almost) completely absent for DD-PC1 and DD-MEδ.

(ii) Available experimental data (separation energies, Q_α values and α-decay half-lives) on SHEs are described with comparable accuracy in covariant (current manuscript) and nonrelativistic [82] DFT calculations. Moreover, these data are not very sensitive to the details of the single-particle structure which define the position of the center of the island of stability. Unfortunately, experimental data on single-particle states in odd-mass SHEs are either not available ($Z \geqslant 105$) or scarce ($100 < Z < 105$). In addition,

in the latter case, the configuration assignments for many nuclei are not fully reliable [86]. However, the analysis of the available data on deformed single-particle states in the actinides performed with different DFTs in Refs. [38,39] reveals that the problems in the description of the single-particle structure exist in all models. Considering the existing theoretical spreads, it is clear that the available experimental data on SHEs do not make it possible to distinguish between the predictions of different models with respect of the position of the center of the island of stability.

(iii) Comparing different functionals, one can see that the results obtained with the covariant density functional DD-MEδ differ substantially from the results of other functionals. This functional is different from all the other functionals used here, because it has been adjusted in Ref. [22] using only four phenomenological parameters in addition to some input from *ab initio* calculations [87,88]. Above $Z = 102$ it does not predict spherical SHEs. The heights of the inner fission barriers in SHEs with $Z = 112$–116 obtained in this functional are significantly lower than the experimental estimates and the values calculated in all other models. In addition, it does not lead to octupole deformation in actinide nuclei which are known to be octupole deformed [31]. All these facts suggest that either the *ab initio* input [87,88] for this functional is not precise enough or the number of only four phenomenological parameters (fitted to masses of spherical nuclei) is too small to provide a proper extrapolation to the region of SHEs. Thus, this functional is not recommended for future investigations in this area, in spite of the fact that this functional provides a good description of masses and other ground-state observables in the $Z \leqslant 104$ nuclei [3].

(iv) Theoretical uncertainties in the predictions of different observables have been quantified. While the uncertainties in the quadrupole deformation of the ground states of known superheavy nuclei are small, they increase on approaching nuclei with $Z = 120$ and/or $N = 184$. As a result, even the ground-state deformations of these nuclei (whether spherical or oblate) cannot be predicted with certainty. Available experimental data do not make it possible to discriminate between these predictions.

TABLE II. The RHB predictions for ground-state properties of even-even nuclei obtained with PC-PK1. Columns 3, 4, and 5 list binding energies E, proton (β_p), and neutron (β_p) quadrupole deformations, respectively. The charge radii r_{ch}, root-mean-square (rms) proton radii r_{rms}^p, and neutron skin thicknesses r_{skin} are presented in columns 6, 7, and 8, respectively. The notation $r_{rms}^p = \langle r_p^2 \rangle^{1/2}$ is used. Note that the neutron rms radii can be calculated as $r_{rms}^n = r_{rms}^p + r_{skin}$. The last column gives α-decay half-lives obtained by means of the Viola-Seaborg formula (see Sec. VIII for details).

| Z | N | E (MeV) | β_p | β_n | r_{ch} (fm) | r_{rms}^p (fm) | r_{skin} (fm) | $\log_{10}(t_\alpha)$ (s) |
1	2	3	4	5	6	7	8	9
118	170	−2034.295	0.168	0.163	6.287	6.236	0.150	−6.731
118	172	−2049.224	0.000	0.000	6.271	6.220	0.153	−6.287
118	174	−2064.100	0.000	0.000	6.278	6.227	0.166	−4.563
118	176	−2078.333	0.000	0.000	6.285	6.233	0.180	−2.755
118	178	−2092.081	0.000	0.000	6.291	6.240	0.192	−1.385
118	180	−2105.365	0.000	0.000	6.297	6.246	0.206	−1.147
118	182	−2118.141	0.000	0.000	6.302	6.251	0.221	−1.152
118	184	−2130.160	0.000	0.000	6.307	6.256	0.236	−1.873
118	186	−2140.809	0.000	0.000	6.329	6.278	0.241	−4.035
118	188	−2151.145	0.000	0.000	6.350	6.299	0.246	−3.289
118	190	−2161.846	−0.400	−0.395	6.603	6.555	0.223	−0.900
118	192	−2172.715	−0.407	−0.403	6.623	6.574	0.234	2.559
118	194	−2183.257	−0.413	−0.411	6.643	6.595	0.244	3.462
118	196	−2193.479	−0.420	−0.419	6.666	6.617	0.253	4.458

APPENDIX : SUPPLEMENTAL INFORMATION ON THE GROUND-STATE PROPERTIES

In addition to the graphical representation of the results, the numerical results for ground-state properties obtained with the DD-PC1 and PC-PK1 CEDFs are provided in two tables of the Supplemental Material with this article as Ref. [89]. The structure of these tables is illustrated in Table II.

[1] J. Erler, N. Birge, M. Kortelainen, W. Nazarewicz, E. Olsen, A. M. Perhac, and M. Stoitsov, Nature (London) **486**, 509 (2012).

[2] A. V. Afanasjev, S. E. Agbemava, D. Ray, and P. Ring, Phys. Lett. B **726**, 680 (2013).

[3] S. E. Agbemava, A. V. Afanasjev, D. Ray, and P. Ring, Phys. Rev. C **89**, 054320 (2014).

[4] Y. T. Oganessian *et al.*, Phys. Rev. C **74**, 044602 (2006).

[5] Y. T. Oganessian *et al.*, Phys. Rev. Lett. **109**, 162501 (2012).

[6] S. G. Nilsson, J. R. Nix, A. Sobiczewski, Z. Szymański, S. Wycech, C. Gustafson, and P. Möller, Nucl. Phys. A **115**, 545 (1968).

[7] S. G. Nilsson, C. F. Tsang, A. Sobiczewski, Z. Szymański, S. Wycech, C. Gustafson, I.-L. Lamm, P. Möller, and B. Nilsson, Nucl. Phys. A **131**, 1 (1969).

[8] Z. Patyk and A. Sobiczewski, Nucl. Phys. A **533**, 132 (1991).

[9] S. Ćwiok, J. Dobaczewski, P.-H. Heenen, P. Magierski, and W. Nazarewicz, Nucl. Phys. A **611**, 211 (1996).

[10] P. Möller and J. R. Nix, J. Phys. G **20**, 1681 (1994).

[11] K. Rutz, M. Bender, T. Bürvenich, T. Schilling, P.-G. Reinhard, J. A. Maruhn, and W. Greiner, Phys. Rev. C **56**, 238 (1997).

[12] M. Bender, K. Rutz, P.-G. Reinhard, J. A. Maruhn, and W. Greiner, Phys. Rev. C **60**, 034304 (1999).

[13] A. V. Afanasjev, T. L. Khoo, S. Frauendorf, G. A. Lalazissis, and I. Ahmad, Phys. Rev. C **67**, 024309 (2003).

[14] W. Zhang, J. Meng, S. Zhang, L. Geng, and H. Toki, Nucl. Phys. A **753**, 106 (2005).

[15] A. V. Afanasjev and S. Frauendorf, Phys. Rev. C **71**, 024308 (2005).

[16] P.-G. Reinhard, M. Rufa, J. Maruhn, W. Greiner, and J. Friedrich, Z. Phys. A **323**, 13 (1986).

[17] G. A. Lalazissis, J. König, and P. Ring, Phys. Rev. C **55**, 540 (1997).

[18] G. A. Lalazissis, T. Nikšić, D. Vretenar, and P. Ring, Phys. Rev. C **71**, 024312 (2005).

[19] T. Nikšić, D. Vretenar, and P. Ring, Phys. Rev. C **78**, 034318 (2008).

[20] G. A. Lalazissis, S. Karatzikos, R. Fossion, D. P. Arteaga, A. V. Afanasjev, and P. Ring, Phys. Lett. B **671**, 36 (2009).

[21] P. W. Zhao, Z. P. Li, J. M. Yao, and J. Meng, Phys. Rev. C **82**, 054319 (2010).

[22] X. Roca-Maza, X. Viñas, M. Centelles, P. Ring, and P. Schuck, Phys. Rev. C **84**, 054309 (2011).

[23] M. Kortelainen, J. McDonnell, W. Nazarewicz, E. Olsen, P.-G. Reinhard, J. Sarich, N. Schunck, S. M. Wild, D. Davesne, J. Erler, and A. Pastore, Phys. Rev. C **89**, 054314 (2014).

[24] S. Goriely, S. Hilaire, M. Girod, and S. Péru, Phys. Rev. Lett. **102**, 242501 (2009).

[25] R. D. Herzberg and P. T. Greenlees, Prog. Part. Nucl. Phys. **61**, 674 (2008).

[26] Y. T. Oganessian and V. K. Utyonkov, Rep. Prog. Phys. **78**, 036301 (2015).

[27] D. Vretenar, A. V. Afanasjev, G. A. Lalazissis, and P. Ring, Phys. Rep. **409**, 101 (2005).

[28] Q. S. Zhang, Z. M. Niu, Z. P. Li, J. M. Yao, and J. Meng, Front. Phys. **9**, 529 (2014).

[29] A. V. Afanasjev, S. E. Agbemava, D. Ray, and P. Ring, Phys. Rev. C **91**, 014324 (2015).

[30] V. Prassa, T. Nikšić, G. A. Lalazissis, and D. Vretenar, Phys. Rev. C **86**, 024317 (2012).

[31] S. Agbemava, A. V. Afanasjev, and P. Ring (unpublished).

[32] H. Abusara, A. V. Afanasjev, and P. Ring, Phys. Rev. C **85**, 024314 (2012).

[33] S. Ćwiok, P.-H. Heenen, and W. Nazarewicz, Nature (London) **433**, 705 (2005).

[34] V. Prassa, T. Nikšić, and D. Vretenar, Phys. Rev. C **88**, 044324 (2013).

[35] P. Möller, R. Bengtsson, B. Carlsson, P. Olivius, T. Ichikawa, H. Sagawa, and A. Iwamoto, At. Data Nucl. Data Tables **94**, 758 (2008).

[36] J. B. Snyder, W. Reviol, D. G. Sarantites, A. V. Afanasjev, R. V. F. Janssens, H. Abusara, M. P. Carpenter, X. Chen, C. J. Chiara, J. P. Greene, T. Lauritsen, E. A. McCutchan, D. Seweryniak, and S. Zhu, Phys. Lett. B **723**, 61 (2013).

[37] A. V. Afanasjev, P. Ring, and J. König, Nucl. Phys. A **676**, 196 (2000).

[38] A. V. Afanasjev and S. Shawaqfeh, Phys. Lett. B **706**, 177 (2011).

[39] J. Dobaczewski, A. V. Afanasjev, M. Bender, L. M. Robledo, and Y. Shi, arXiv:1504.03245 [Nucl. Phys. A (to be published)].

[40] W. Koepf and P. Ring, Phys. Lett. B **212**, 397 (1988).

[41] Y. K. Gambhir, P. Ring, and A. Thimet, Ann. Phys. (NY) **198**, 132 (1990).

[42] P. Ring, Y. K. Gambhir, and G. A. Lalazissis, Comp. Phys. Commun. **105**, 77 (1997).

[43] T. Nikšić, N. Paar, D. Vretenar, and P. Ring, Comp. Phys. Commun. **185**, 1808 (2014).

[44] Y. Tian, Z. Y. Ma, and P. Ring, Phys. Lett. B **676**, 44 (2009).

[45] J. F. Berger, M. Girod, and D. Gogny, Comp. Phys. Commun. **63**, 365 (1991).

[46] A. V. Afanasjev and O. Abdurazakov, Phys. Rev. C **88**, 014320 (2013).

[47] P. G. Reinhard and W. Nazarewicz, Phys. Rev. C **81**, 051303(R) (2010).

[48] J. Dobaczewski, W. Nazarewicz, and P.-G. Reinhard, J. Phys. G **41**, 074001 (2014).

[49] B. G. Todd-Rutel and J. Piekarewicz, Phys. Rev. Lett. **95**, 122501 (2005).

[50] J. J. Li, W. H. Long, J. Margueron, and N. V. Giai, Phys. Lett. B **732**, 169 (2014).

[51] G. A. Lalazissis, S. Karatzikos, M. Serra, T. Otsuka, and P. Ring, Phys. Rev. C **80**, 041301 (2009).

[52] E. Litvinova and P. Ring, Phys. Rev. C **73**, 044328 (2006).

[53] E. V. Litvinova and A. V. Afanasjev, Phys. Rev. C **84**, 014305 (2011).

[54] A. V. Afanasjev and E. Litvinova, Phys. Rev. C **92**, 044317 (2015).

[55] E. Litvinova, Phys. Rev. C **85**, 021303(R) (2012).

[56] M. Bender, W. Nazarewicz, and P.-G. Reinhard, Phys. Lett. B **515**, 42 (2001).

[57] V. M. Strutinsky, Yad. Fiz. **3**, 614 (1966).

[58] V. M. Strutinsky, Nucl. Phys. A **95**, 420 (1967).

[59] V. M. Strutinsky, Nucl. Phys. A **122**, 1 (1968).

[60] S. G. Nilsson and I. Ragnarsson, *Shapes and Shells in Nuclear Structure* (Cambridge University Press, Cambridge, U.K., 1995).

[61] P. Ring and P. Schuck, *The Nuclear Many-Body Problem* (Springer-Verlag, Berlin, 1980).

[62] Z. Ren, H. Toki, Z. Ren, and H. Toki, Nucl. Phys. A **689**, 691 (2001).

[63] T. Bürvenich, M. Bender, J. A. Maruhn, and P.-G. Reinhard, Phys. Rev. C **69**, 014307 (2004).

[64] B.-N. Lu, J. Zhao, E.-G. Zhao, and S.-G. Zhou, Phys. Rev. C **89**, 014323 (2014).

[65] B.-N. Lu, E.-G. Zhao, and S.-G. Zhou, Phys. Rev. C **85**, 011301 (2012).

[66] J. Zhao, B.-N. Lu, D. Vretenar, E.-G. Zhao, and S.-G. Zhou, Phys. Rev. C **91**, 014321 (2015).

[67] M. Kowal, P. Jachimowicz, and A. Sobiczewski, Phys. Rev. C **82**, 014303 (2010).

[68] P. Möller, A. J. Sierk, T. Ichikawa, A. Iwamoto, R. Bengtsson, H. Uhrenholt, and S. Åberg, Phys. Rev. C **79**, 064304 (2009).

[69] A. Staszczak, A. Baran, and W. Nazarewicz, Phys. Rev. C **87**, 024320 (2013).

[70] M. Warda and J. L. Egido, Phys. Rev. C **86**, 014322 (2012).

[71] P. Jachimowicz, M. Kowal, and J. Skalski, Phys. Rev. C **83**, 054302 (2011).

[72] A. V. Afanasjev and S. E. Agbemava, Acta Phys. Pol. B **46**, 405 (2015).

[73] Evaluated Nuclear Structure Data File (ENSDF) located at the web site (http://www.nndc.bnl.gov/ensdf/) of Brookhaven National Laboratory. ENSDF is based on the publications presented in Nuclear Data Sheets (NDS), which is a standard for evaluated nuclear data.

[74] G. Agbemava, A. V. Afanasjev, T. Nakatsukasa, and P. Ring (unpublished).

[75] M. Wang, G. Audi, A. H. Wapstra, F. G. Kondev, M. MacCormick, X. Xu, and B. Pfeiffer, Chin. Phys. C **36**, 1603 (2012).

[76] G. Audi, M. Wang, A. H. Wapstra, F. G. Kondev, M. MacCormick, X. Xu, and B. Pfeiffer, Chin. Phys. C **36**, 1287 (2012).

[77] A. Sobiczewski, I. Muntian, and Z. Patyk, Phys. Rev. C **63**, 034306 (2001).

[78] A. Sobiczewski and K. Pomorski, Prog. Part. Nucl. Phys. **58**, 292 (2007).

[79] T. Bürvenich, K. Rutz, M. Bender, P.-G. Reinhard, J. A. Maruhn, and W. Greiner, Eur. Phys. J. A **3**, 139 (1998).

[80] Y. Shi, J. Dobaczewski, and P. T. Greenlees, Phys. Rev. C **89**, 034309 (2014).

[81] G. Audi, F. Kondev, M. Wang, B. Pfeiffer, X. Sun, J. Blachot, and M. MacCormick, Chin. Phys. C **36**, 1157 (2012).

[82] M. Bender, P.-H. Heenen, and P.-G. Reinhard, Rev. Mod. Phys. **75**, 121 (2003).

[83] J. V. E. Viola and G. T. Seaborg, J. Inorg. Nucl. Chem. **28**, 741 (1966).

[84] T. Dong and Z. Ren, Eur. Phys. J A. **26**, 69 (2005).

[85] X. Bao, H. Zhang, H. Zhang, G. Royer, and J. Li, Nucl. Phys. A **921**, 85 (2014).

[86] H. B. Jeppesen *et al.*, Phys. Rev. C **80**, 034324 (2009).

[87] M. Baldo, C. Maieron, P. Schuck, and X. Viñas, Nucl. Phys. A **736**, 241 (2004).

[88] E. N. E. van Dalen, C. Fuchs, and A. Faessler, Eur. Phys. J. A **31**, 29 (2007).

[89] See Supplemental Material at http://link.aps.org/supplemental/10.1103/PhysRevC.92.054310 for the tables with the results of the calculations based on the DD-PC1 and PC-PK1 CEDFs.